Monthly Notices
of the
ROYAL ASTRONOMICAL SOCIETY

MNRAS **485,** 3409–3429 (2019)
Advance Access publication 2019 February 28

doi:10.1093/mnras/stz564

Widespread star formation inside galactic outflows

R. Gallagher,[1,2]★ R. Maiolino,[1,2]★ F. Belfiore,[3] N. Drory,[4] R. Riffel[5,6] and R. A. Riffel[6,7]

[1]*Cavendish Laboratory, University of Cambridge, 19 J. J. Thomson Ave., Cambridge CB3 0HE, UK*
[2]*Kavli Institute for Cosmology, University of Cambridge, Madingley Road, Cambridge CB3 0HA, UK*
[3]*University of California Observatories – Lick Observatory, University of California Santa Cruz, 1156 High Str, Santa Cruz, CA 95064, USA*
[4]*McDonald Observatory, The University of Texas at Austin, 2515 Speedway Stop C1402, Austin, TX 78712, USA*
[5]*Departamento de Astronomia, Av. Bento Goncalves 9500, Agronomia, Porto Alegre, RS 91501-970, Brazil*
[6]*Laboratório Interinstitucional de e-Astronomia, Rua General José Cristino, 77 Vasco da Gama, Rio de Janeiro 20921-400, Brazil*
[7]*Departamento de Fisica, Universidade Federal de Santa Maria, CEP 97105-900 Santa Maria, RS, Brazil*

Accepted 2019 January 31. Received 2019 January 28; in original form 2018 June 21

ABSTRACT

Several models have predicted that stars could form inside galactic outflows and that this would be a new major mode of galaxy evolution. Observations of galactic outflows have revealed that they host large amounts of dense and clumpy molecular gas, which provide conditions suitable for star formation. We have investigated the properties of the outflows in a large sample of galaxies by exploiting the integral field spectroscopic data of the large MaNGA-SDSS4 galaxy survey. We find evidence for prominent star formation occurring inside at least 30 per cent of the galactic outflows in our sample, whilst signs of star formation are seen in up to half of the outflows. We also show that even if star formation is prominent inside many other galactic outflows, this may have not been revealed as the diagnostics are easily dominated by the presence of even faint active galactic nucleus and shocks. If very massive outflows typical of distant galaxies and quasars follow the same scaling relations observed locally, then the star formation inside high-z outflows can be up to several 100 $M_{\odot}$ yr^{-1} and could contribute substantially to the early formation of the spheroidal component of galaxies. Star formation in outflows can also potentially contribute to establishing the scaling relations between black holes and their host spheroids. Moreover, supernovae exploding on large orbits can chemically enrich *in situ* and heat the circumgalactic and intergalactic medium. Finally, young stars ejected on large orbits may also contribute to the reionization of the Universe.

Key words: galaxies: active – galaxies: evolution – galaxies: formation – galaxies: kinematics and dynamics – galaxies: starburst.

1 INTRODUCTION

Fast outflows, extending on kiloparsec scales, are commonly found in galaxies hosting enhanced star formation ('starburst') and in galaxies hosting accreting supermassive black holes [BHs; quasars or, more generally, active galactic nuclei (AGNs)]. Galactic outflows are often invoked as a negative feedback process in galaxies; indeed, by removing and heating gas, outflows can potentially suppress star formation in their host galaxies (e.g. Granato et al. 2004; King 2010; Fabian 2012; King & Pounds 2015). However, some models have also proposed that outflows and jets can also have a positive feedback effect; indeed, compressing gas in the interstellar and circumgalactic galactic outflows can foster the fragmentation and gravitational collapse of clouds, hence boost star formation (Rees 1989; Nayakshin & Zubovas 2012; Zubovas et al. 2013a; Bieri et al. 2016). However, more recently, models have proposed an even more fascinating scenario, according to which the outflowing gas should cool, fragment and, therefore, form stars *inside* the outflow (Gaibler et al. 2012; Ishibashi & Fabian 2012, 2014; Ishibashi, Fabian & Canning 2013; Silk 2013; Zubovas et al. 2013b; Dugan et al. 2014; Zubovas & King 2014; El-Badry et al. 2016; Mukherjee et al. 2018; Wang & Loeb 2018). This new star formation mode is drastically different from star formation in galactic discs and even from star formation resulting from the 'standard' positive feedback scenario discussed above. Indeed, stars formed inside galactic outflows would have high velocities on nearly radial orbits. Depending on the radius and velocity at the time of formation, stars born inside outflows may escape the galaxy and/or the halo, or become gravitationally bound (Zubovas et al. 2013c). According to models,

★ E-mail: rmg55@cam.ac.uk (RG); r.maiolino@mrao.cam.ac.uk (RM)

this star formation mode can reach a few/several 100 $M_\odot$ yr^{-1} (Ishibashi & Fabian 2012; Silk 2013). The implications of this new star formation mode are potentially far reaching, ranging from the morphological/dynamical evolutionary properties of galaxies to the enrichment of the circumgalactic and intergalactic medium (IGM), as will be discussed in more detail in Section 7.

Observations have recently shown that fast galactic outflows contain a large amount of cold molecular gas (e.g. Feruglio et al. 2010; Sturm et al. 2011; Cicone et al. 2014; Combes et al. 2014; Sakamoto et al. 2014; Garcia-Burillo et al. 2015; Fluetsch et al. 2018), including an unusually high fraction of dense molecular gas (Aalto et al. 2012, 2015; Privon et al. 2017; Walter et al. 2017), which is also found to be highly clumpy (Borguet et al. 2012; Finn et al. 2014; Pereira-Santaella et al. 2016). These observational results provide strong support to the theoretical scenario in which star formation occurs in galactic outflows, since these possess the physical conditions (cold, dense, and clumpy gas) suitable for star formation.

Several clear examples of star formation triggered in shocked and compressed gas clouds have been unambiguously seen in our Galaxy (Zavagno et al. 2010a,b; Brand et al. 2011; Dewangan et al. 2012; Thompson et al. 2012; Dewangan & Ojha 2013; Deharveng et al. 2015; Ladeyschikov et al. 2015; Duronea et al. 2017; Dwarkadas et al. 2017; Figueira et al. 2017; Baug et al. 2018; Lim et al. 2018). On larger scales, evidence for star formation triggered by the interaction of jets or outflows with the interstellar medium or CGM of galaxies has also been detected, although the inferred star formation rate (SFR) is generally low ($< 1 M_\odot$ yr^{-1}; Croft et al. 2006; Elbaz et al. 2009; Crockett et al. 2012; Cresci et al. 2015b; Salomé, Salomé & Combes 2015; Santoro et al. 2016; Lacy et al. 2017; Molnár et al. 2017). At high-redshift indications of star formation triggered by outflows or radio jets has also been found in some cases potentially reaching a few hundred $M_\odot$ yr^{-1} (Bicknell et al. 2000; Cresci et al. 2015a). However, all these cases are examples of the 'standard' positive feedback mode, in which star formation is triggered as a consequence of the compression of the interstellar/circumgalactic medium (CGM) resulting from the interaction with the jet/outflows.

Evidence for the new mode of positive feedback, i.e. star formation *inside* galactic outflows, has been found only recently by Maiolino et al. (2017). They analysed optical/near-IR spectroscopic data of the prominent galactic outflow previously detected in the galaxy IRAS F23128-5919 (Piqueras López et al. 2012; Bellocchi et al. 2013; Arribas et al. 2014; Leslie et al. 2014; Cazzoli et al. 2016) and found that multiple optical and near-IR diagnostics of the outflowing gas are consistent with *in situ* star formation, i.e. inside the outflow. However, whilst this has been a remarkable result, it has not been clear whether this is an isolated, rare case, or star formation is more common in galactic outflows, but it has been difficult to identify.

Indeed, outflows are often driven by AGNs, which (as we shall discuss in Section 6) tend to dominate the diagnostics, especially in integrated or nuclear spectra, and the presence of shocks may also hinder the detection of star formation.

We have investigated the occurrence of this phenomenon in a systemic and unbiased way by exploiting the integral field spectra of the 2800 galaxies of the MaNGA-SDSS4 DR2 survey. These offer high quality, spatially resolved spectra spanning a broad wavelength range, hence enabling us to probe multiple diagnostics. We identify a subsample of 37 galaxies that show evidence for clear outflows and which can be traced through all primary nebular lines required for identifying the sources of gas ionization/excitation through diagnostic diagrams. We have therefore exploited these data to map the diagnostics across each outflow, hence revealing the presence of star formation inside outflows. As we will discuss in detail, we have found that about one third of outflows are characterized by prominent star formation inside them, and about half of the outflows show evidence for at least some star formation, hence revealing that star formation is common to most galactic outflows, with major implications especially for high-redshift galaxies, where outflows are much more prominent.

In this paper, we assume the following cosmological parameters: $H_0 = 70$ km s^{-1} Mpc^{-1}, $\Omega_\Lambda = 0.7$, and $\Omega_m = 0.3$.

2 DATA ANALYSIS

2.1 The MaNGA survey

The observations for the Sloan Digital Sky Survey (SDSS)-IV MaNGA survey (Bundy et al. 2015; Blanton et al. 2017) are taken on the Sloan 2.5m telescope (Gunn et al. 2006), using hexagonal Integral Field Unit (IFU) fibre bundles, ranging from 19 to 127 fibres in size, with 17 galaxies observed simultaneously. These IFUs feed the light into the dual-channel BOSS spectrographs (Drory et al. 2015). The size of the fibre bundle is chosen to ensure coverage out to a minimum of 1.5 Re for the MaNGA primary sample, and 2.5 Re for the secondary sample. The observing strategy chosen utilizes a three-point dithering pattern, with a total exposure time per galaxy of around 3 hr, aiming to reach the MaNGA requirement of signal-to-noise ratio (SNR) of 5 per spectral pixel in the *r*-band continuum at a surface brightness of 23 AB arcsec^{-2}. Each set of exposures is also required to provide a median seeing of 2.0 arcsec or below, providing a Point Spread Function (PSF) of less than 3 arcsec in the reconstructed images (Law et al. 2015, 2016; Yan et al. 2016b,a).

The wavelength coverage in the MaNGA cubes ranges from 3600 to 10300 Å at $R \sim 2000$, providing simultaneous access to the nebular lines [O II]$\lambda\lambda$3727, 3730; Hβ; [O III]$\lambda\lambda$4959, 5007; [O I]$\lambda\lambda$6300, 6366; [N II]$\lambda\lambda$6548, 6584; Hα; and [S II]$\lambda\lambda$6717, 6731. These are fundamental nebular lines that can be used to investigate the excitation and physical properties of the ionized gas. In particular, the so-called BPT diagnostic diagrams (Baldwin, Phillips & Terlevich 1981; Kewley et al. 2006) compare the ratios of different nebular emission lines (specifically: [O III]λ5007/Hβ versus [N II]λ6584/Hα, [S II]λ6717 + 6731/Hα, and [O I]λ6300/Hα) to enable a classification in terms of sources responsible for ionizing and exciting the gas, specifically differentiating between excitation from young hot stars in star-forming regions and other forms of excitation such as AGNs, evolved stellar populations and shocks.

2.2 Spectral fitting, identification, and mapping of outflows

We have considered all IFU spectra of the 2800 galaxies in the MaNGA DR2. Since outflows [both AGN driven and SF driven] are generally more prominent in the central region of galaxies, we have first inspected the spectrum of the central region of the galaxy, i.e. extracted from the central 2.5 arcsec (which corresponds to the typical PSF of the Sloan 2.5 m Telescope), with the goal of identifying candidate galaxies showing indication of outflows. One aside to the decision for this scale is that, due to the MaNGA galaxies spanning a range of redshifts, this area from which we extract our 'central' spectrum will correspond to a different physical scale on each galaxy.

The first step was to fit the stellar continuum in this central region. For this purpose, we used the full MILES empirical stellar library, consisting of 985 stellar templates. Unfortunately, this library only covers the wavelength range of 3525–7500 Å, hence not fully exploiting the full coverage of the MaNGA data, which extends up to 10 000 Å. However, it covers the continuum beneath all nebular lines of interest, and has a spectral resolution high enough to match the MaNGA spectra. The fitting of the continuum was done by using an adapted version of the PPXF routine (Cappellari 2017).

We begin the analysis of the central spectrum by fitting the stellar continuum and kinematics, whilst also masking all nebular emission lines within $\pm$1000 km s^{-1} from each line's redshifted central wavelength. The continuum is fit using the PPXF routine, assuming four Lines Of Sight Velocity Distribution (LOSVD) components (v, σ, h3, and h4), and allowing a sixth-order additive Legendre polynomial to correct the continuum shape for small residual background. The [O II]λ5577 sky line is also masked, as although good sky subtraction has been performed on the MaNGA data, some residuals can still exist for this line.

Having fit the stellar continuum, the residual spectrum from the fit was next tested for multiple emission line components. To investigate the presence of multiple components in the emission lines, we began by testing the primary nebular lines mentioned above. We first simultaneously fit all nebular lines with a single Gaussian component, imposing the same central velocity and width for all nebular lines. The intensities of the Gaussian components of the individual nebular lines were left free to vary, with the exception of the [N II], [O III], and [O I] doublets, whose line ratios were tied by their Einstein coefficients.

Note that when tying the velocity dispersions, one has to take into account that the spectral resolution changes slightly across the MaNGA spectrum. However, the latter is very well characterized in each spectral region and provided together with each spectrum. Therefore, at each point we can link the intrinsic velocity dispersion/width (which is to be tied for all lines) to the observed velocity width through the relation

$$\sigma_{\rm line} = \sqrt{\sigma^2_{\rm SRES} + \sigma^2_{\rm int}},$$

where $\sigma_{\rm line}$ is the dispersion of the final Gaussian fit, $\sigma_{\rm SRES}$ is the spectral resolution at the observed wavelength of the line, and $\sigma_{\rm int}$ is the tied dispersion between all lines.

Following this, we then investigated the presence of a second, broader component of the nebular lines. Assuming the emission lines could be well modelled by Gaussian templates, we allowed up to two Gaussians to be fit to each emission line, fitting only the first two orders of the LOSVD (i.e. velocity and dispersion).

In type-1 AGNs, the very broad emission lines from the broad line region (BLR) make it difficult to characterize the outflow; therefore, we have decided to discard this class of galaxies. Type-1 AGNs were identified as galaxies with nuclear very broad hydrogen Balmer lines [typically with full width at half-maximum (FWHM) ranging from 1000 to 10 000 km s^{-1}] without an associated broad component of the forbidden transitions (in particular [O III] and [S II]), which indicate that the broad Balmer component is indeed associated with the BLR and not outflow.

The putative additional (broader) Gaussian component was also required to have the same velocity and width for all nebular lines, with only the intensity of the broad component of the individual nebular lines left free to vary, though with the same constraints on the line doublets as discussed above. For our pipeline to accept a second component, we require a number of conditions to be met. The most basic condition is that the multiple components fit improved upon the reduced chi-squared of the single-component fit by a minimum of 10 per cent. This is always a very conservative requirement, as with so many spectral points this always translates into a statistical significance of the additional component higher than 99 per cent. In principle, one could relax this requirement, but, in this paper, we have preferred to be conservative in the identification of the broad components.

We also place two restrictions upon the broad components for both the Hα and [O III]λ5007 lines. First, we require that the SNR (defined by the peak flux of the fitted Gaussian divided by the median error within the FWHM of the line) is greater than 3. Secondly, we require that the equivalent width of the broad component (relative to the total continuum) must also be greater than 3. These requirements are put in place to ensure that the broad component is a distinct feature, separate from the narrow component and not simply an artefact of poor stellar continuum fittings. In a later discussion within this paper, we mention how we cannot disentangle the stellar continuum of the constituent stars in the galaxy from those being formed within outflows, preventing us from separating the true equivalent width associated with the outflowing (broad) components. However, in the context of this section we are now mostly focused on the operational identification of the broad component and making sure that it is not resulting, as already discussed above, from an inappropriate subtraction of the stellar continuum, hence we consider the equivalent width of the broad component relative to the total stellar continuum. In many of the cases, the restriction on the SNR is strict enough that spurious sources are removed without consideration of the equivalent width regardless. In practice, for this specific paper, these requirements are overridden by the subsequent requirements of detecting also the broad component of the fainter lines required for the BPT classifications. Any galaxy that exhibits a broad component that meets both of these requirements is considered to be an outflow candidate for further consideration.

The broad component of [O I]λ6300 is often very weak and often undetected. However, generally, when non-detected the upper limit on [O I]λ6300 is meaningful, in the sense that it locates the broad component in the H II-like (star-forming) region of the [O I]-BPT diagram.

Having positively identified multiple components in a spectrum, we next performed a check to ensure the emission line masks provided in the first steps are sufficiently masking the emission lines. We define a line a being sufficiently masked if the mask covers out to 3σ from each line centre (using the updated values of line centres and widths). Insufficient masks can lead to poor recovery of the stellar kinematics. Thus, if any of the lines are broader than their initial masks, then the masks are moved and increased in size to sufficiently mask the line, and the stellar kinematics are refit as before, and emission lines tested again. This step is repeated iteratively until the reduced chi squared of the continuum fit does not improve upon the previous fit's reduced chi squared. At this point, the stellar kinematics are assumed good, are saved, and held fixed in all future steps.

In the next stage of the fitting process, the stellar continuum is fit again, with fixed kinematics, whilst simultaneously fitting the emission lines, whose kinematics were free to vary. This method was chosen as it has been previously shown that line fluxes can be underestimated by as much as 10 per cent when fit post-continuum subtraction (Sarzi et al. 2006). With some of our lines being relatively low flux (especially for Hβ), we indeed found that in cases

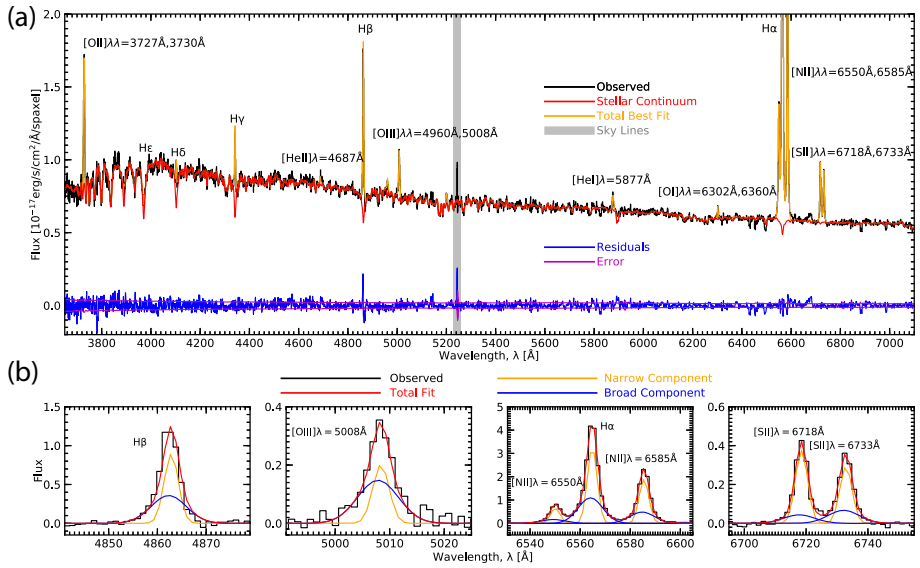

Figure 1. Example of simultaneous stellar continuum and emission-line fit to the spectrum extracted from the central region of a representative galaxy in our sample. (a) Full spectrum decomposition showing the simultaneous stellar continuum (red) and emission-line (orange) fit to spectrum. Shown below the fit are the residuals (blue) and the error spectrum (magenta) for the galaxy. The O II 5577 sky line has been masked, shown here by the grey shaded area. (b) Subsections of continuum-subtracted spectra, showing some of the relevant emission lines used in the analyses. The decomposition of the narrow (orange) and broad (blue) components can be seen, alongside the total fit of the two components (red).

where the fit was performed post subtraction, the continuum fit itself was sometimes modified by PPXF to account for template mismatch through the additive polynomials used to correct for continuum shape. In these situations, the simultaneous fitting of the continuum and the emission lines alleviated the problem.

Fig. 1 shows the spectral fitting of the central region of a representative galaxy resulting from the steps described above.

For those galaxies showing evidence for an outflow in the central spectrum, we then extend the map of the associated broad components across the entire galaxy.

We begin by estimating the continuum SNR of each spaxel. This was determined by taking the medians of the flux and inverse variance spectra, provided in the MaNGA cubes, within the SDSS R band ($5560 < \lambda < 6942$ Å). All spaxels with SNR < 5 were removed at this point, as the spaxels were to be binned to higher SNR, and these spaxels would lead to large bins with noisy data.

Taking the remaining spaxels, all of the spectra were first collapsed into a single integrated spectrum. This was fit using similar steps as discussed above, and the non-zero weighted templates extracted to create individual template libraries for each galaxy, typically reducing the full MILES library from 985 to 25–40 templates that best described the galaxy properties. This was done to speed up the fitting process, typically by an order of magnitude.

Next, the spaxels were Voronoi binned to increase the SNR of the continuum for the binned spectra to 25. Through the use of Monte Carlo simulations, it was determined that a minimum SNR of 25 should be used for a sufficiently accurate recovery of the stellar kinematics (Sarzi et al. 2006). The high SNR binned spectrum is used to restrict the number of templates to be used for the stellar fitting within the bin and to provide the initial parameters for fitting the stellar kinematics and for the nebular lines. Then the latter information is used to fit each individual spaxel within the Voronoi bin, by following the same steps discussed above for the central spectrum.

Fig. 2(a) shows the kinematics of the narrow (disc) and broad (outflow) components, along with the stellar kinematics, for the same representative galaxy analysed in Fig. 1. The same figure shows the flux distribution of both the narrow and broad components of both the H α and [O III]λ5007 lines. The same flux maps have been obtained also for the other lines required for the BPT diagram.

This analysis could be performed for a total of 37 MaNGA galaxies. This does not mean that other galaxies in the MaNGA data do not show outflows, but that only for these 37 galaxies were all of the lines required for BPT analysis prominent, and that the outflowing gas could be kinematically separated from the constituent gas of the galaxy disc, allowing for a clean and detailed analysis of the outflow using BPT diagnostics.

The list of the 37 galaxies with outflows that can be characterized through the BPT diagnostics is given in Table A1, along with their stellar masses from the MPA-JHU catalogue (Brinchmann et al. 2004).

The fitting results and maps (including the BPT maps for the narrow components) for the full set of 37 MaNGA galaxies for which this analysis has been possible are available in electronic form in the accompanying supplementary online material.

Finally, we mention that the fluxes of the nebular emission lines, both narrow and broad, were corrected for dust reddening by assuming the default Calzetti et al. (2000) attenuation curve and using the H α/H β ratio to infer reddening.

2.3 Investigating the effects of beam smearing

A potential problem of the modest angular resolution of the MaNGA data is that the putative broad component in the innermost, central region may simply be an artefact of beam smearing of the rotation in the central region. Many authors explore this issue by modelling the rotation curve and then simulating the effect of the beam smearing; however, such a test is dependent on the model adopted to describe

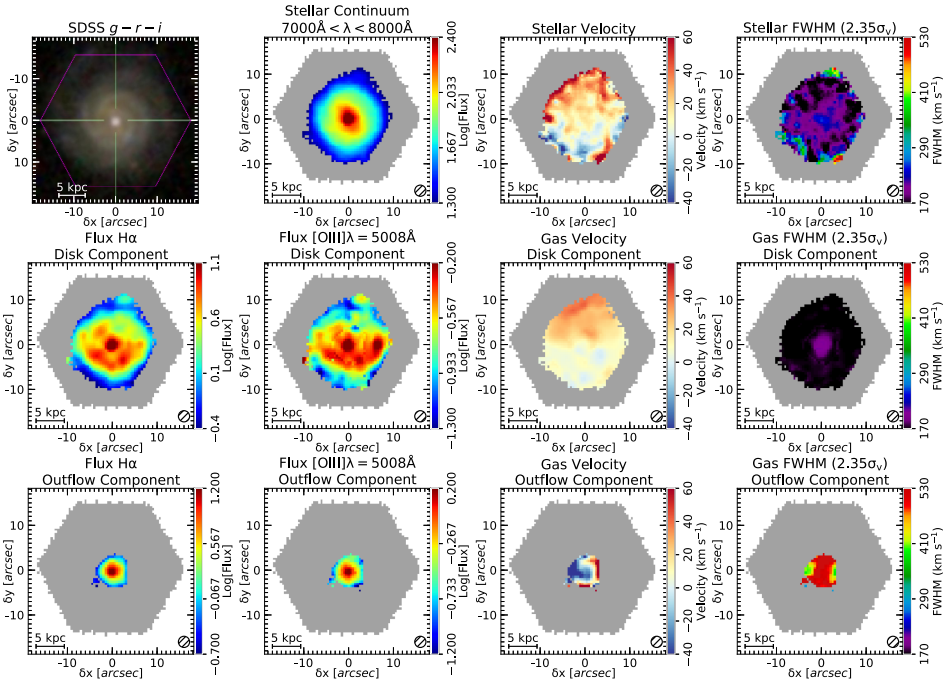

Figure 2. Example multicomponent mapping. For the same representative galaxy of Fig. 1, the panels show flux, velocity, and velocity dispersion maps for the stellar population, for the narrow component of the nebular lines, tracing the galactic disc, and for the broad component of the nebular lines, tracing the outflow. The grey regions indicate spaxels within the Manga fibre bundle footprint but masked because either the stellar continuum or emission-line component is not detected.

the velocity field in the central region; therefore, to avoid being model dependent, we have not used this method.

Instead, we have simply compared the velocity dispersion of the broad component in the central region with the central stellar velocity dispersion, which is affected by the same beam smearing. A broadening resulting from beam smearing of the stellar velocity field should result in the stellar velocity dispersion being as high as the broad component of the gas. Fig. 3 shows comparisons of the central velocity dispersion of both the narrow (left) and broad (right) gas components with the stellar velocity dispersion. The narrow components tend to show a similar dispersion as the stars (the solid line represents the 1:1 ratio), and in some cases a smaller dispersion, as the gaseous disc is typically dynamically cooler than the stars in the bulge (e.g. Bertola et al. 1995; Corsini et al. 1999; Young, Bureau & Cappellari 2008; Martinsson et al. 2013). Conversely, the broad components are always found to have a dispersion much larger than the stellar component (the dashed line represents the 2:1 ratio), indicating that the broadening cannot originate from beam smearing. This further indicates that the broad component is tracing gas not in virial equilibrium with the gravitational field, which is traced by the old stellar population, hence implying that the broad component is truly tracing outflowing material. A further indication that the broad component is not resulting from effects of beam smearing is the fact that such component is not distributed along the minor axis of rotation (which instead is a typical signature of broadening by beam smearing of the rotation field), whilst it is well extended also fully resolved along the major axis direction. The fact that the outflow is resolved is further confirmed by the fact that the broad components have clear kinematic structures both in the velocity map and in the dispersion map.

3 FRACTION OF OUTFLOWS HOSTING STAR FORMATION

3.1 Spatially resolved BPT-diagnostics

We have explored the properties of the outflow by investigating the spatially resolved BPT diagrams of the outflow in each galaxy. We recall that these diagrams enable the classification of galactic regions in terms of gas excitation/ionization mechanisms, specifically, star formation (i.e. H II region excited by young, massive hot stars), excitation by supermassive accreting BHs (i.e. Seyfert or Quasar nuclei), and low ionization nuclear emission line regions (LINERs). The latter is a class of object comprising a broad range of excitation mechanisms: initially, it was proposed that they are associated with excitation by weak, radiatively ineffcient accreting BHs (e.g. Ho, Filippenko & Sargent 1993); however, it has been realized that in most local galaxies the 'LINER' emission is generally extended on kpc-scales across a large fraction of passive and green valley galaxies (hence renaming this class as 'LIER', i.e. dropping the 'N' which stands for 'Nuclear' in the original acronym) and correlates with the old stellar population, and this can be explained in terms of excitation by the hard radiation field produced by evolved post-AGB stars (e.g. Sarzi et al. 2010; Belfiore et al. 2016). However, in some active galaxies and outflows, the LI(N)ER emission can also be associated with shocks excitation (e.g. Heckman, Armus & Miley 1987; Monreal-Ibero et al. 2010). A more detailed discussion on the origin of the LI(N)ER emission goes beyond the scope of this paper.

Fig. 4(a) shows the line of demarcation between the different excitation mechanisms identified by Kauffmann et al. (2003), Kewley et al. (2001), and Kewley et al. (2006) in the three

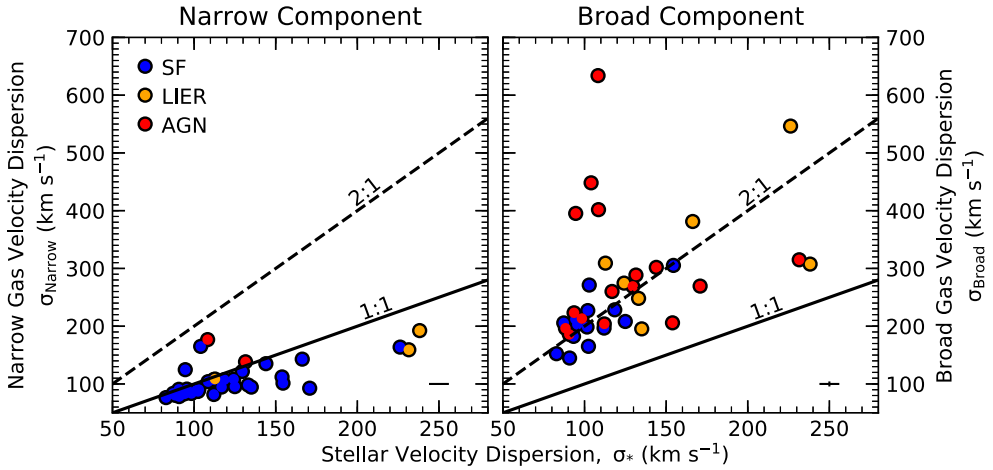

Figure 3. Left: Velocity dispersion of the narrow component of the nebular lines in the central region compared with the stellar velocity dispersion. As expected, the narrow component has a velocity dispersion similar to the stellar velocity dispersion, or even lower, owing to the fact that the gas disc is generally dynamically colder than stars. Right: Velocity dispersion of the broad component of the nebular lines in the central region compared with the stellar velocity dispersion in the same region. The former is much larger than the latter, indicating that the broad component cannot result from beam smearing effects of the central rotation curve and that it must be associated with non-virial motions, i.e. outflows.

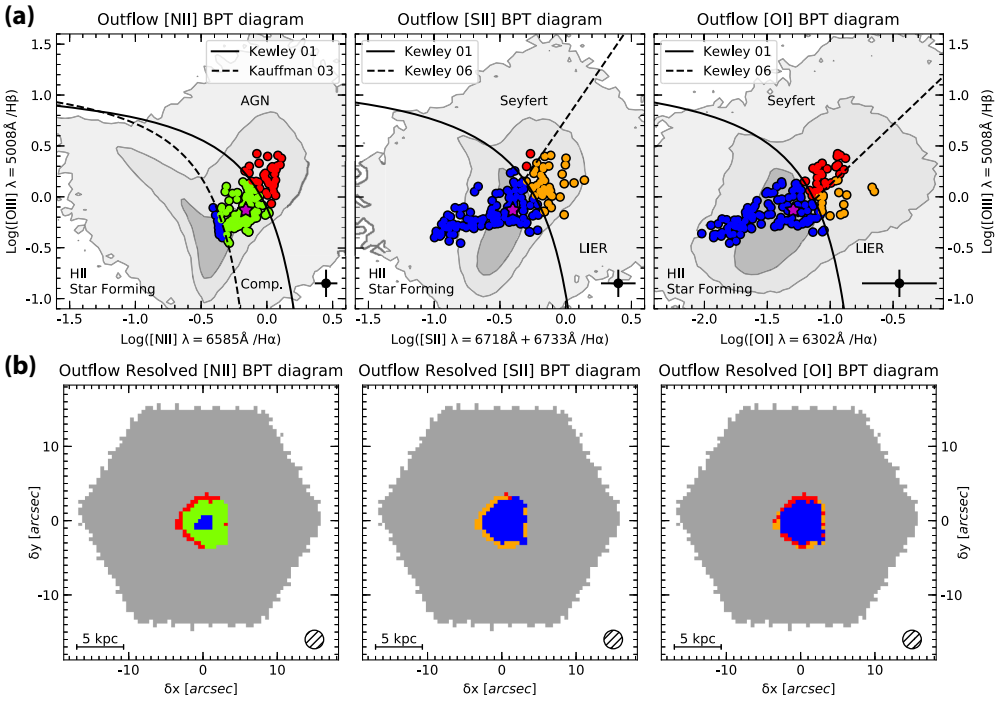

Figure 4. (a) Distribution of the broad (outflow) component of the nebular lines on the BPT diagrams for the same representative galaxy of Figs 1 and 2. A significant fraction of this galactic outflow is in the BPT regions typically populated by star-forming regions and star-forming galaxies. The magenta star shows the median location of the BPT points in the outflow. The background grey-scale contours indicate the distribution of several hundred thousand galaxies in the SDSS survey. (b) Spatially resolved BPT classification of the outflowing gas, using the same colour coding as in (a). The central region of the outflow is mostly star forming, whilst towards the outer parts of the outflow excitation by shocks likely dominates. Maps for the other 37 galaxies, including BPT maps for the narrow components, can be found in the supplementary material.

BPT diagrams. The grey shaded contours show the distribution of several hundred thousands galaxies in the SDSS (single fibre) DR7 survey (the distribution of spatially resolved MaNGA spaxels for the full survey is broadly consistent with the single-fibre DR7 data; however, we prefer to use the latter as the MaNGA spaxels underpopulate the AGN locus, Belfiore et al. 2016). On the [N II]-BPT diagram, the Seyfert/quasars and LI(N)ER are not clearly divided and are generally classified together as 'AGN'. On the same diagram, Kauffmann et al. (2003) identified a demarcation curve between H II/star-forming regions and AGNs (dashed line)

empirically based on the distribution of galaxies in the SDSS survey, whilst (Kewley et al. 2001) provided a curve (solid line) tracing the maximum line ratios associated with star-forming regions according to photoionization models; galaxies/regions in the area between these two curves are often referred to as 'composite' systems, in which both SF and AGN probably coexist. However, we shall note that objects in this region are still fully compatible with the maximum line ratios expected from star-forming galaxies, hence they can still be fully star forming.

We note that other diagnostic diagrams involving the equivalent width of Hα (Cid Fernandes et al. 2011) cannot be used in this case, as we cannot discriminate the continuum associated with the broad and narrow components. Therefore, in this paper, we only exploit the BPT diagrams to identify the excitation mechanism in galactic regions and specifically in the outflows.

As an example of BPT diagnostics spatially resolved in outflows, Fig. 4(a) shows the BPT classification of the broad (outflow) component of each individual spaxel of the same representative galaxy shown in representative galaxy (Fig. 2). The representative error bars shown in the bottom right show the median errors for each of the ratios (where the errors are determined from the errors returned on the fit to the velocities, velocity dispersions, and fluxes for each line). Fig. 4(b) shows how the BPT classification is distributed within the outflow map. For this galaxy, both the [S II]-BPT and [O I]-BPT diagrams consistently indicate that the central region of the outflow is star formation dominated, whilst shocks likely dominate in the outer regions of the outflow. The [N II]-BPT diagram also provides a consistent picture if one includes 'composite' spaxels (green) as hosting star formation, since, as discussed above, objects in this region of the BPT diagram can still potentially be fully star forming. One should also take into account that the [N II]-BPT diagram is considered as the least reliable of such diagrams because of its strong dependence on the nitrogen abundance (Masters, Faisst & Capak 2016) and on the ionization parameter (Strom et al. 2018).

To have a useful quantities of comparison for the outflow in the different galaxies in our sample, we condense the information on each outflow by taking the median location on the BPT diagram of such outflow components for each galactic outflow. In the case of the galaxy shown in Fig. 4(a), the median location in each BPT diagram is shown with a magenta star symbol. We note that this is a considerable improvement, enabled by spatially resolved spectroscopy, relative to spatially integrated spectra, which are generally light-weighted and therefore dominated by the brightest regions (e.g. a central AGN-dominated region).

Fig. 5 shows the resulting median location of the outflows on the BPT diagrams for all systems in our sample (Table A2 gives the average BPT classification for each individual object). The [S II]-BPT and [O I]-BPT diagrams indicate that in most outflows the ionized gas appears to be excited by AGN; however, about 30 per cent of the outflows host gas whose ionization is dominated by young stars. For the [N II]-BPT, a smaller fraction of outflows appear dominated by star formation excitation. However, if one also includes outflows whose [N II]-BPT classification is in the 'composite' region (considered as a transition region in which star formation and AGN excitation coexists), then the fraction of outflows showing indication of star formation increases to about 30 per cent also in the [N II]-BPT diagram. One should also take into account the concerns about the [N II]-BPT diagram discussed above.

Even for those galactic outflows whose median BPT diagnostics are associated with AGN or LIER-like ionization, there are generally still regions of the outflow that are associated with star formation. Therefore, to better quantify the occurrence of star formation in galactic outflows, we have estimated for each outflow the fraction of spaxels that can be classified as 'star forming' according to each of the BPT diagnostics. Fig. 6 shows the distribution of galaxies as a function of the fraction of the outflow that is classified as star forming. According to the [S II]-BPT and [O I]-BPT classifications, about half of the galactic outflows show evidence for some star formation inside the outflow (whose contribution to the overall excitation of the gas ranges from 10 per cent to 100 per cent). Even the [N II]-BPT diagram provides the same fraction of 'star-forming outflows' if one considers also outflowing regions classified as 'composite' in this diagram.

3.2 *In situ* versus external photoionization

One potential concern of our finding could be that, for those outflowing regions where the BPT diagnostics of the outflowing gas are consistent with excitation from young stars, the latter may not be located inside the outflow but in the galactic disc, and the outflowing gas may simply be illuminated externally by the UV radiation coming from the disc. However, these scenarios can be distinguished by exploiting the ionization parameter, defined as ratio between ionizing photons flux ($Q_{\rm ion}/4\pi r^2$) and gas electronic density ($n_{\rm e}$), and normalized through the speed of light,

$$U = \frac{Q_{\rm ion}}{4\pi r^2 c\, n_{\rm e}}.$$

The gas density in the outflow is similar, or even higher than in the disc, as inferred from the [S II] doublet (Gallagher et al. in preparation). Therefore, in the scenario of external photoionization, one would expect that the ionizing flux should be much lower than in the case of *in situ* photoionization, therefore resulting into an ionization parameter orders of magnitude lower than observed in standard star-forming regions.

The ionization parameter can be traced through the [O III]λ5007/[O II]λ3727 line ratio (Díaz et al. 2000). This ratio has however also a secondary dependence on the gas metallicity. The latter can however be monitored through the R_{23} parameter defined as the ratio $([{\rm O\,III}]_{4960+5007} + [{\rm O\,II}]_{3727})/{\rm H}\,\beta$, which is primarily sensitive to the oxygen abundance, and with a secondary dependence on the ionization parameter. Therefore, diagrams with both these two quantities are used to help disentangling these properties (e.g. Nagao, Maiolino & Marconi 2006).

Fig. 7 shows the [O III]λ5007/[O II]λ3727 ratio as a function of the R_{23} parameter. The right-hand axis translates the [O III]λ5007/[O II]λ3727 ratio into U following the relation provided by Díaz et al. (2000). The shaded contours indicate the distribution of star-forming galaxies from the SDSS survey (68 per cent, 95 per cent, and 99.7 per cent of the population), illustrating the well-known correlation between U and metallicity (e.g. Nagao et al. 2006). Dark blue symbols indicate the median values observed in the galactic outflows of our sample that are dominated by star formation, according to the [S II]-BPT diagnostic diagram, as in Fig. 5, whilst light blue symbols show the medial location of the narrow component tracing star formation in the galaxy disc. Fig. 7 shows that the ionization parameter of the gas in the star-forming outflows, as inferred from the [O III] λ5007/[O II] λ3727 line ratio, is undistinguishable from that of normal star-forming regions/galaxies and, if anything, is even slightly higher. This result excludes that the photoionization in these outflows is due to external

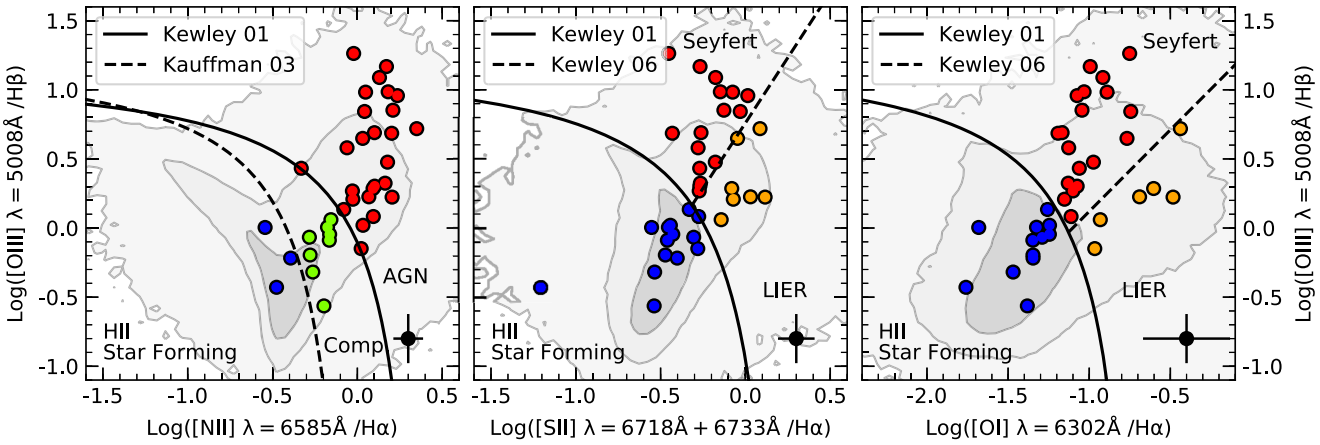

Figure 5. Median BPT classification of the outflows for the galaxies in our sample. According to their median BPT classification in the [S II] and [O I] diagrams (central and right panes), about 30 per cent of the galactic outflows in our sample are 'star forming'. The same applies to the [N II] classification if one includes galaxies classified as 'composite' (however, one should take into account that the [N II] classification is more ambiguous, as discussed in the text).

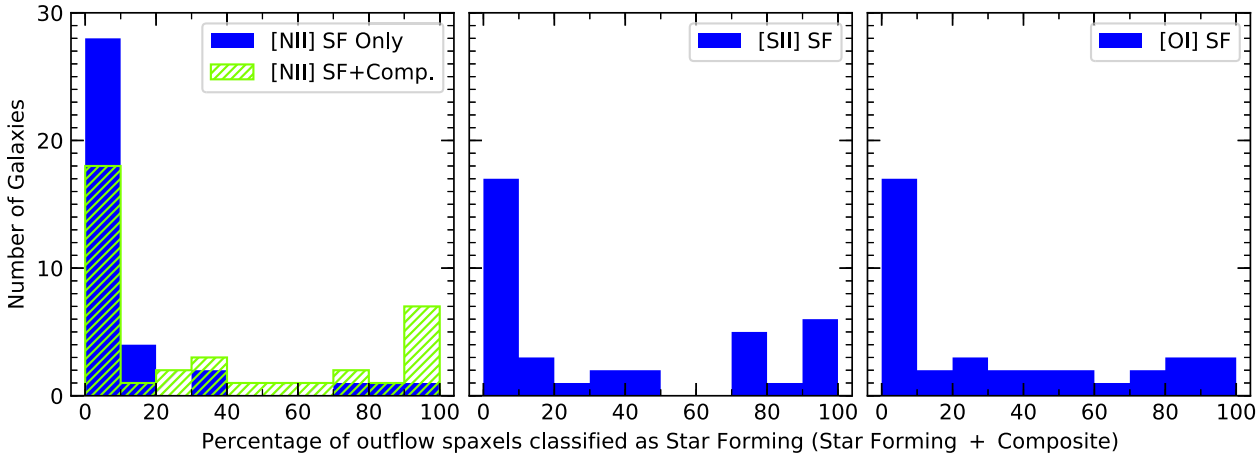

Figure 6. Distribution of the outflows as a function of their star-forming fraction. Each panel shows the distribution of outflows that have a given fraction of spaxels classified as star forming according to each of the three BPT diagrams. In the case of the [N II]-BPT, the combined case of 'star forming' and 'composite' is also shown. According to the [S II] and [O I] classifications, about half of the outflows have at least 10 per cent of the spaxels that are star forming. The same result applies to the [N II] classification if one includes the composite cases.

UV radiation coming from the star-forming disc, and confirming that the outflowing gas is excited by *in situ* (i.e. within the outflow) star formation.

3.3 Contribution by shocks

One caveat to using both the BPT diagrams and the R_{23} versus O_{32} diagram in identifying *in situ* star formation lies in the fact that, although generally shocks populate the LIER-like region of these diagram (e.g. Allen et al. 2008; Diniz et al. 2017), some peculiar shocks (especially low velocity ones) can potentially produce star-formation-like emission line ratios on the BPT diagrams. In Maiolino et al. (2017), this form of potential shock excitation was excluded through the use of IR diagnostics, namely the [Fe II] λ1.64 μm/Brγ versus H_2(1–0)S(1)/Brγ and [Fe II] λ1.25 μm/Paβ versus [P II] λ1.18 μm/Paβ diagrams, afforded by the extended IR wavelength coverage offered by the X-shooter data. Unfortunately, the MaNGA wavelength coverage stops at ∼10 000 Å, hence preventing their use for disentangling star formation in these galaxies.

However, we have investigated whether such shocks can potentially mimic star formation-like line ratios observed by us in galactic outflows by employing the MAPPINGS III library of fast radiative shock models (Allen et al. 2008). The predictions of extensive grids of these models, spanning a wide range of velocities and physical parameters, have been overlayed on the BPT diagrams and on the R_{23} versus O_{32} diagram, together with the location of the line ratios observed in the Manga outflows. These various plots are shown in the Appendix. Not unexpectedly, shock models can reproduce well several line ratios in the LIER region, as well as in the AGN-Seyfert regions. However, although some shock models do overlap with the loci occupied by star-forming regions, the vast majority of the line ratios observed in the star-forming outflows identified by us (blue symbols) are inconsistent with the shock models, further reinforcing the claim that we are indeed observing star formation inside these outflows.

The additional issue with shocks is that they are much less effective in producing ionizing photons than young, hot stars, hence much less likely to account for the large nebular luminosities observed in the outflow. Assuming a typical radius of the putative shocked region

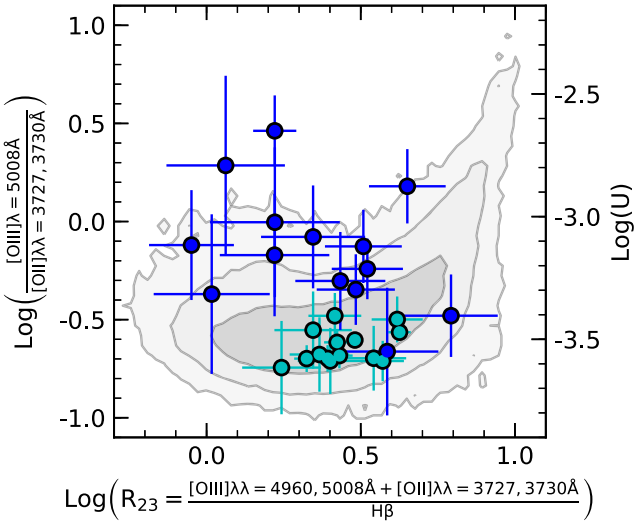

Figure 7. Ionization parameter (right-hand *Y*-axis) as traced by the [O III]/[O II] ratio (left-hand *Y*-axis) as a function of the R_{23} parameter, which is primarily sensitive to the gas metallicity. Dark blue symbols indicate the median values observed in those galactic outflows dominated by star formation, according to the [S II]-BPT diagnostic diagram, as in Fig. 5. The light blue symbols are the average location of the narrow component in regions that are classified as star forming. The shaded contours indicate the distribution of star-forming galaxies from the SDSS survey (68 per cent, 95 per cent, and 99.7 per cent of the population). Star-forming outflows (blue symbols) have similar ionization parameter as normal star-forming regions, and possibly even slightly higher. The error bars shown are the median error of the ratios calculated for all spaxels within the outflow.

of ∼3 kpc (as inferred from our maps), by using the equations given in Allen et al. (2008), focusing on slow shocks ($\upsilon_s \sim 100$ km s^{-1}), which are the ones that may mimic star-forming like line ratios, and assuming the extreme (unrealistic) case of shocked gas covering the entire 4π solid angle with covering factor of unity, we infer that the expected ionizing photon luminosity should be about $Q_{\rm ion} \approx 10^{52}$ s^{-1}. Assuming that these photons are entirely absorbed by the gas (by ionizing it), this would result into a Hα luminosity of the outflowing gas of $\sim 10^{40}$ erg s^{-1}. Much more realistically, the putative shocked gas is characterized by a much smaller solid angle (outflows, when observed at high angular resolution have typically solid angles less than π, e.g. Venturi et al. 2018), with small covering factor (0.02–0.2, e.g. Baskin & Laor 2005) and only a fraction of the ionizing photons is likely absorbed by the outflowing clouds, hence resulting in to an expected Hα luminosity one or two orders of magnitude lower, i.e. $\sim 10^{38}$–10^{39} erg s^{-1}. Except for one case, all outflows that we have classified as star forming have a Hα luminosity in the range of 10^{40}–10^{41} erg s^{-1}, hence very unlikely to be produced by shocks.

The combination of these energetics arguments and the location of shock models on the diagnostic diagrams discussed above provide strong evidence against any significant role of shocks in the ionization of the outflows that we have identified as hosting star formation.

4 SFR INSIDE OUTFLOWS

4.1 Contribution to the total star formation

For those outflows showing evidence for star formation, we can estimate the SFR by using the broad component of Hα as a tracer of star formation (Kennicutt & Evans 2012). The SFRs inferred in these local outflows are of the order of 0.1–1 M$_\odot$ yr^{-1} (Table A2). In Fig. 8, we compare the SFR inside the outflow with the total SFR of the galaxy, as inferred by the total Hα emission (both narrow and broad), integrated across the entire galaxy (excluding AGN and LIER-like regions). Star formation in the outflow contributes 'only' between 5 per cent and 30 per cent to the total SFR of these local galaxies (with one extreme case dominating the total SFR).

However, in the spaxels where multiple components are detected (typically within the central few kpc), the star formation inside the outflow can dominate the local SFR. This is illustrated in Fig. 9,

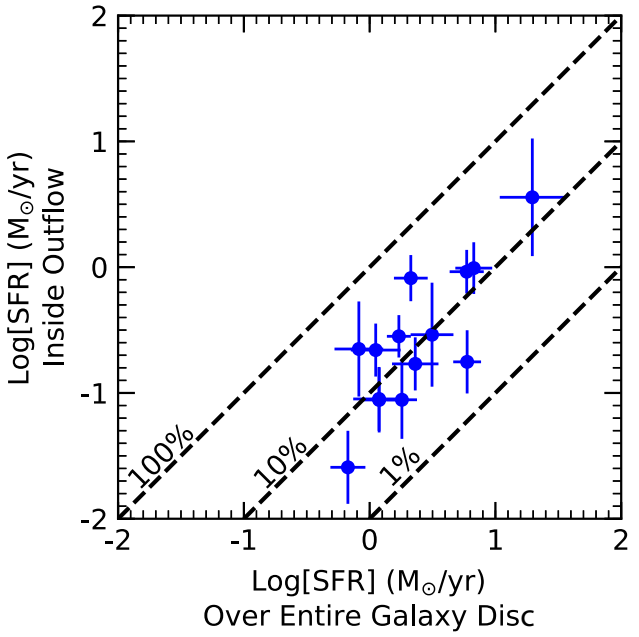

Figure 8. SFR inside the outflow as a function of total SFR in the disc of the host galaxy.

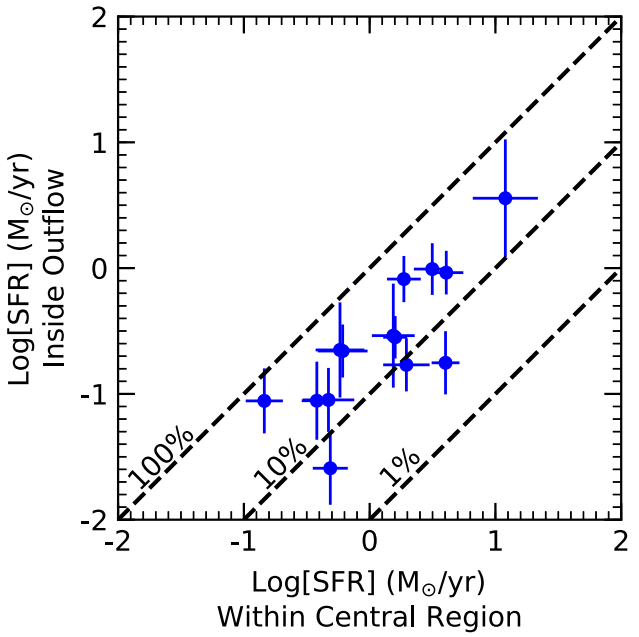

Figure 9. SFR inside the outflow as a function of the SFR in the same central projected area in which the outflow is detected.

where the SFR inside the outflow is compared with the SFR in the region in which the outflow is detected (i.e. where a broad component is detected, which is generally in the central region).

These SFRs are certainly modest and may be regarded as currently not very relevant for galaxy evolution. However, one should also take into account that these are relatively mild outflows, whilst star formation may be much more prominent inside the massive outflows driven by massive star-forming galaxies at high redshifts or powerful distant quasars. To investigate this possibility in the following, we explore the scaling relation between star formation inside the outflow and mass outflow rate.

4.2 Ionized outflow rate

Unfortunately, we only have information on the ionized component of the outflowing gas, therefore we can only obtain information on the ionized gas outflow rate. The ionized phase generally accounts for a small fraction of the total gas content in outflows (Carniani et al. 2015; Fiore et al. 2017; Fluetsch et al. 2018); however, it can be used as a proxy of the global outflow rate.

We have adopted a method similar to the one described by Carniani et al. (2015) and Cicone et al. (2015). More specifically, for each point where we detect an outflow component we estimate the contribution to the outflow rate as the mass of ionized gas at that point divided by the dynamical time from the centre:

$$\dot{M}_{\rm outf-ion} = \frac{M_{\rm outf-ion}}{\tau_{\rm dyn}} = \frac{M_{\rm outf-ion}\ v_{\rm outfl.}}{R_{\rm outfl}},$$

where $v_{\rm outfl}$ is the outflow velocity at that location, which we define as $|v| + {\rm FWHM}/2$ of the broad component ($|v|$ being the absolute velocity of the centre of the broad component tracing the outflow, relative to the galaxy rest frame), $R_{\rm outfl}$ is the distance of the specific location to the galaxy centre (within the central PSF region this is taken as the size of the PSF, which actually gives a lower limit to the contribution to the outflow rate in this region) and $M_{\rm outfl\text{-}ion}$, is the mass of ionized gas at that location (spaxel). Projection effects, resulting from the direction of the outflowing gas relative to the line of sight, affect both the observed velocity and the observed radius. However, it can be easily shown (Cicone et al. 2015) that the correction factor, averaged over the entire 4π solid angle, is 1; therefore, statistically, projection effects do not plague results, although they certainly introduce scatter. Assuming $T_{\rm e} \sim 10^4$ K, the mass of ionized gas in the outflow at that location is given by the luminosity of the [O III]λ5007 emission at the same location through the following relation:

$$M_{\rm out\text{-}ion,[O\,III]} = 2 \times 10^8\,{\rm M}_\odot\ 10^{-[{\rm O/H}]} \times \left(\frac{L_{\rm [O\,III]}}{10^{44}\ {\rm erg\ s^{-1}}}\right)\left(\frac{n_{\rm e}}{200\ {\rm cm^{-3}}}\right)^{-1},$$

where [O/H] is the oxygen abundance relative to solar and $n_{\rm e}$ is the electron density in the outflow, which we have assumed to be 200 cm^{-3}, which is intermediate between the results obtained by Perna et al. (2017) (for AGN-driven outflows) and the result obtained by Genzel et al. (2014) (for outflow in massive star-forming galaxies). In a future work (Gallagher et al. in preparation), we will refine the outflow rates by taking the gas density inferred directly from the sulphur doublet at each location of each outflow.

Alternatively, the mass of the ionized outflow can be inferred from the broad component of Hα from the following equation

$$M_{\rm out\text{-}ion,H\,\alpha} = 1.5\ 10^9\,{\rm M}_\odot \left(\frac{L_{\rm H\alpha}}{10^{44}\ {\rm erg\ s^{-1}}}\right)\left(\frac{n_{\rm e}}{200\ {\rm cm^{-3}}}\right)^{-1}.$$

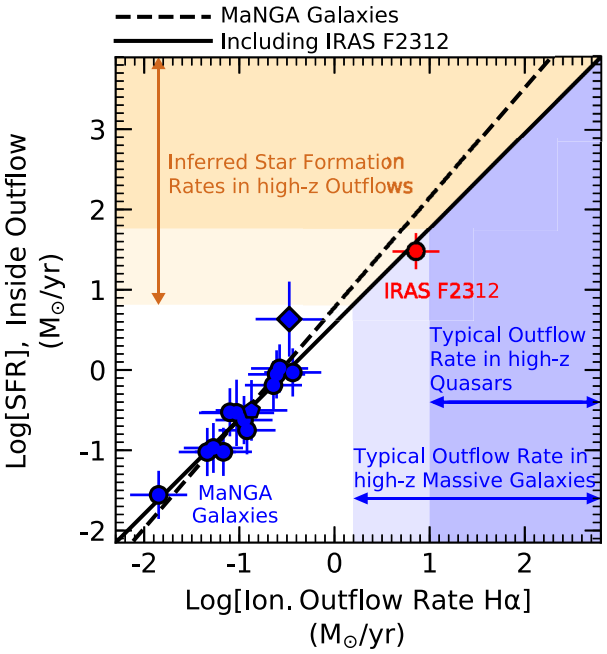

Figure 10. SFR inside the outflow as a function of ionized gas mass outflow rate inferred from the Hα. Blue symbols are star-forming outflows in local MaNGA galaxies studied in this paper. The red symbol indicates the star-forming outflow previously detected in IRAS F23128-5919 (Maiolino et al. 2017). The dashed line shows the fit to the MaNGA outflows presented in this paper (blue points). The solid line is the linear fit including IRAS F23128-5919 (equation 2). The blue shaded regions indicate the ionized outflow rate inferred for high-z massive galaxies and quasars. The orange shaded regions indicates the SFR inside these distant galactic outflows if they follow the same correlation observed locally.

As already pointed out by Carniani et al. (2015), if assuming solar metallicity, the outflow mass inferred from [O III] broad component gives an outflow rate which is about a factor of ~3–5 lower than inferred from Hα or Hβ. This is either because the gas metallicity may be lower than solar or, more likely, because [O III] does not account for the contribution from lower ionization stages of oxygen.

In either cases, the total outflow rate was then obtained by summing the individual contributions to the outflow rate of all individual spaxels.

4.3 Scaling relations and implications for high-redshift galaxies

We have explored the connection between outflow rate and star formation in the outflow.

We have initially focused the outflow rate inferred from the Hα broad component, because less subject to ionization and metallicity corrections. For those galaxies whose outflow is dominated by star formation in terms of BPT diagnostics, Fig. 10 shows the SFR inside the outflow as a function of the ionized outflow rate estimated from the broad component of Hα. Blue symbols are star-forming outflows discovered in this paper, whilst the red symbol is the star formation previously discovered inside the outflow of the galaxy IRAS F23128-5919 (Maiolino et al. 2017). The data reveal a clear correlation between the two quantities. To perform linear fits to the data, accounting for the errors in both the outflow rate and SFR, we used the `scipy` Orthogonal Distance Regression (ODR) package. The errors in these quantities were calculated through rigorous error

propagation, though we elected to maintain a minimum error or 0.3 dex to account for previous considerations, such as assuming density values of 200 cm^{-3} and LOSVD errors being the formal errors on the fit returned from `mpfit`. We began by performing a fit to the MaNGA outflows presented in this paper alone. This fit is shown by the dashed line, and extrapolation of this fit is nicely consistent with the star formation observed in the outflow of IRAS F23128-5919. This fit takes the form

$$\log(\mathrm{SFR_{outfl}}) = 1.37(\pm0.14)\ \log(\dot{M}_{\mathrm{outfl\text{-}ion,H}\alpha}) + 0.77(\pm0.14). \quad (1)$$

Including the latter galaxy in a secondary fit results in the fit shown by the solid line, which is only slightly different from the fit to the MaNGA galaxies alone, and takes the form:

$$\log(\mathrm{SFR_{outfl}}) = 1.19(\pm0.07)\log(\dot{M}_{\mathrm{outfl-ion,H}\alpha}) + 0.58(\pm0.07). \quad (2)$$

We recall again that generally the ionized outflow rate is a small fraction of the total outflow rate (especially relative to the molecular phase). The blue shaded regions indicate the ionized outflow rate inferred for high-z massive galaxies and quasars, as inferred from Hα or Hβ data (Carniani et al. 2015; Genzel et al. 2014; Fiore et al. 2017). The orange shaded regions indicate the SFR inside these distant galactic outflows if they follow the same correlation observed locally, implying SFRs in outflows ranging from $\sim$10 $M_\odot$ yr^{-1} up to $\sim$1000 $M_\odot$ yr^{-1}, which would certainly contribute significantly to the galaxy formation, and to their spheroidal component in particular.

Such high SFRs in distant galactic outflows may have been missed by past observing campaigns, and in Section 6, we will discuss the possible reasons for this.

One potential problem of the diagram in Fig. 10 is that the broad H α flux is a quantity used to measure both the ionized outflow rate (together with the additional information on the outflow velocity and distribution) and to estimate the SFR in the outflow, which may induce a spurious correlation. Therefore, in order to test whether the correlation persist even by adopting different tracers that use independent quantities, we have considered the outflow rate estimated through the [O III] line. As discussed above, [O III] is more unreliable as an outflow tracer (because of its dependence on the metallicity and on the ionization degree) and tends to underestimate the outflow rate; however, it has the advantage that it is completely independent of the Hα flux used to estimate the SFR. Fig. 11 shows the star formation in the outflow as a function of the ionized outflow rate as inferred from the broad component of the [O III] line. Again, two fits were performed: first to the MaNGA outflows alone, and secondly to the MaNGA outflows including IRAS F23128-5919 in the fit. The two quantities are still clearly correlated, although the scatter is slightly larger than in Fig. 10. In this case, the fit to the MaNGA outflows alone (dashed line) is less consistent with the outflow in IRAS F23128-5919, and takes the form:

$$\log(\mathrm{SFR_{outfl}}) = 1.32(\pm0.18)\log(\dot{M}_{\mathrm{outfl\text{-}ion,[O\,III]}}) + 2.02(\pm0.37). \quad (3)$$

However, the larger scatter in the data makes the extrapolation of the MaNGA data less reliable. The solid line shows the linear fit including both the MaNGA outflows and the outflow in IRAS F23128-5919, which is given by the following equation

$$\log(\mathrm{SFR_{outfl}}) = 0.92(\pm0.06)\log(\dot{M}_{\mathrm{outfl\text{-}ion,[O\,III]}}) + 1.2(\pm0.1). \quad (4)$$

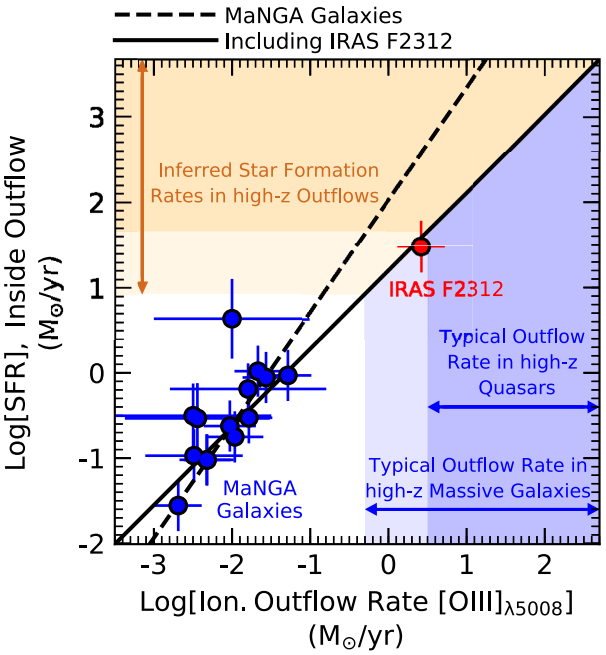

Figure 11. As Fig. 10, but where the ionized outflow rate is now inferred from the broad component of the [O III] line.

The slope, close to unity, is very similar to the slope obtained in equation (2) when using Hα as a tracer of the SFR. The intercept is obviously different, as a consequence of [O III] underestimating the ionized outflow rate. The blue and orange shaded regions in Fig. 11 have the same meaning as in Fig. 10 (in this case the range of outflow rates, based on [O III], in high-z galaxies is more incomplete and we have simply assumed the ranges inferred from Hα an Hβ and shifted by a factor of 0.5 dex, as discussed in Section 4.2). As in the previous case, the extrapolation to the outflow rates of high-redshift galaxies implies high SFRs in the outflows of distant galaxies.

We shall recall that stars obviously form out of the molecular phase of galactic outflows; therefore, it would certainly be more appropriate to exploit scaling relations involving the molecular outflow rate. Unfortunately, information on the molecular outflow rate is not yet available for these star-forming outflows (although ALMA observations are ongoing for some of these systems). However, it should be noted that Fluetsch et al. (2018) have found that the molecular-to-ionized outflow rate increases with AGN luminosity (an opposite trend with respect to what found by Fiore et al. 2017, who however use disjoint samples to probe the ionized and molecular phases, hence potentially subject to differential selection effects); therefore, in powerful outflows driven by luminous AGNs the fraction of stars forming in outflows may potentially be even larger than that inferred from the scaling relations with the ionized component of outflows given by equations (2) and (4).

5 DISTRIBUTION OF GALAXIES WITH OUTFLOWS ON THE SFR–M_* DIAGRAM

The distribution of galaxies on the SFR–M_{star} diagram is often used to identify their properties. Most star-forming galaxies are distributed along the so-called main sequence, a tight relation in which the SFR is nearly proportional to the stellar mass (Renzini & Peng 2015). This is thought to represent the sequence along which galaxies form stars through secular, smooth evolution. Passive

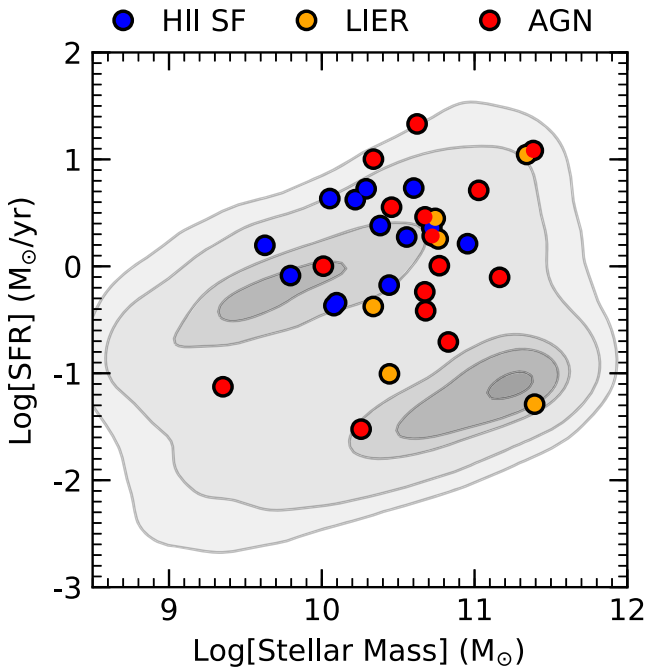

Figure 12. SFR versus stellar mass diagram. The background contour plot shows the distribution of all 2800 galaxies in the MaNGA sample. The symbols show the distribution of galaxies with outflows presented in this study, i.e. those for which the outflows can be analysed in the BPT diagram. The BPT classification of the outflow is the same as in the [S II]-BPT diagram of Fig. 5. Most outflows, especially those hosting star formation inside the outflow, are located around the massive end of the main sequence, or slightly above it.

galaxies have SFRs well below the 'main sequence', whilst galaxies distributed between the main sequence and the passive population (in the region that is often referred to as 'green valley') are believed to be in the process of being quenched or being 'rejuvenated'. The distribution of the 2800 MaNGA galaxies (our parent sample) on the SFR–$M_{\rm star}$ diagram is shown with grey contours in Fig. 12 (SFR and $M_{\rm star}$ are obtained from the DR7 catalogue[1]). The main sequence in this sample is less populated than in other samples (such as, for instance, SDSS-DR8) primarily as a consequence of the MaNGA selection criterion of having a flat distribution in stellar mass. The MaNGA galaxies with outflows investigated in this paper, i.e. those for which the outflow can be studied in terms of BPT diagram, are shown with symbols, which are colour-coded according to the [S II]-BPT classification of the gas in the outflow as in Fig. 5. Most of the galaxies with outflow are distributed around the massive end of the main sequence. Outflows hosting star formation (blue symbols) are along the main sequence or slightly above it. There are some outflows amongst passive and green-valley galaxies, but only with AGN and LIER-like excitation. The lack of outflows in low-mass galaxies may primarily result from selection effects, as these tend to be fainter and are likely characterized by milder outflows (either SF driven or AGN driven), below our detection threshold. A more detailed analysis of the statistical properties of outflows will be discussed in another paper. However, the finding that outflows hosting star formation are located primarily on, or slightly above, the massive end of the main sequence supports the scenario in which this star formation mode may contribute to the population of stars in the bulge; although the overall contribution to the bulge population at this late epoch is minor, the contribution of this mechanism to the evolution of the bulge may have been significant at high z, in the early phase of galaxy formation. This result is in line with the recent finding that galaxies above the main sequence have bluer bulges, which may still be in the process of forming a fraction of their stars (Morselli et al. 2017).

We finally mention that, both morphologically and kinematically, nearly all galaxies showing star formation inside outflows appear to be isolated systems, typically regular galaxy disc. Only two of these galaxies are interacting systems, which are marked with superscript 'a' in Table A1.

6 WHY HAS STAR FORMATION IN OUTFLOWS BEEN ELUSIVE?

If star formation in outflows is as common as inferred in Section 3 and can reach SFRs as high as inferred in Section 4.3 in high-z galaxies, why has this phenomenon remained elusive so far?

One of the primary reasons is that different excitation mechanisms do not have the same weight in affecting the location of galaxies or galactic regions on the BPT diagrams. In particular, in this section we show that even if prominent star formation is taking place inside the outflow, the presence of an even weak AGN photoionizing the gas within the outflow generally dominates these diagnostic diagrams, even in the scenarios with the most conservative assumptions, implying that the fraction of star-forming outflows inferred in Section 3 is actually a lower limit.

To show this, we make two simplifying assumptions: first, we assume that the BH accretion and star formation in the spheroidal component of the galaxy evolve along the local $M_{\rm BH}$–$M_{\rm spheroid}$ relation; secondly, we take the most extreme (and most conservative) case possible, wherein we assume that all stars in the spheroid form through star formation within the outflow.

This implies that

$$\dot{M}_{\rm BH} \approx 5\ 10^{-3}\ {\rm SFR}_{\rm spheroid} \quad (5)$$

(Kormendy & Ho 2013). Assuming a radiative efficiency of 0.1 for BH accretion, the relationship between Hα emission (in the NLR) and X-ray luminosity for type-2 AGNs given in Ueda et al. (2015), and the X-ray to bolometric AGN luminosity correction given in Marconi et al. (2004) [here we take the bolometric correction appropriate for the typical AGN luminosity considered by Ueda et al. (2015) implying $L_{\rm bol}/L_{(2-10\,{\rm keV})} = 20$], we get

$$L_{{\rm H}\alpha}({\rm AGN})[{\rm erg\ s^{-1}}] = 2 \times 10^{42}\ \dot{M}_{\rm BH}\ [{\rm M_\odot\ yr^{-1}}]. \quad (6)$$

By also using the relation between L(H α) and SFR given in Kennicutt & Evans (2012), in combination with equations (5) and (6), we obtain

$$L_{{\rm H}\alpha}({\rm AGN}) \approx 5\ L_{{\rm H}\alpha}({\rm SFR}) \quad (7)$$

and, of course, the same relation applies to Hβ. Moreover, for most local star-forming galaxies typically $L_{[{\rm O\,III}]}({\rm SFR}) \leq L_{{\rm H}\beta}({\rm SFR})$, whilst for AGNs $L_{[{\rm O\,III}]}({\rm AGN}) \approx 10\ L_{{\rm H}\beta}({\rm AGN})$; as a consequence, together with equation (7), this implies that the BPT diagnostics will be totally skewed towards the AGN region on their Y-axis. Similarly, given that [N II], [S II], and [O I] are all more luminous in AGNs than in SF galaxies, together with equation (7), this implies that the BPT diagnostics will be all skewed towards the AGN region also on the X-axis. Therefore, even in the most conservative scenario assumed above, in which the formation of the spheroidal component of the galaxy results entirely from star formation in the

[1] https://wwwmpa.mpa-garching.mpg.de/SDSS/DR7/

outflow, implying prominent star formation in the outflow, such star formation may go entirely undetected in the BPT diagrams as the excitation diagnostics are totally dominated by AGN excitation.

This issue has been clearly directly demonstrated in detailed spatially resolved cases in which star-forming clumps have remained elusive because diagnostics have been dominated by the photoionization of an even weak AGN (Santoro et al. 2016).

One consideration that complicates things further is the presence of shocks. In these cases, the detection of SF is even more difficult as they are expected to move the diagnostics towards the LIER regions on the diagrams.

Summarizing, the lack of star formation-like BPT diagnostics in outflows does not necessarily exclude the presence of star formation inside the outflow, as such outflows may still host prominent star formation but may struggle to be detected as other sources of excitation may be dominating the diagnostics. Star formation inside outflows becomes easier to detect when the AGN has faded away, and when shocks are weak.

The implication in the context of this paper is that the fraction of outflows with star formation may be higher than what estimated in Section 3.

In integrated, spatially unresolved (or poorly resolved) spectra, the light weighting further enhances the bright, central AGN-dominated emission (especially in the case of powerful quasars) relative to weaker star-forming regions. This issue is obviously more problematic at high redshift due to the lower spatial resolution. However, despite of these difficulties, current data already show some indications of star formation in high-redshift outflows. Genzel et al. (2014) investigated the outflows of five high-z galaxies and two of them have diagnostic ratios consistent with star formation inside the outflow.

The finding that at high-redshift star-forming regions tend to shift towards the AGN locus on the BPT diagrams (e.g. Strom et al. 2017) is a further complication that may have led the classification of some outflows as AGN dominated, whilst their BPT ratios may actually be associated with star formation inside the outflow.

Another problem is that often only the [N II]-BPT diagram is used to classify outflows. As discussed in Strom et al. (2018) and Masters et al. (2016), the [N II]-BPT is much more subject to changes in the ionization parameters and nitrogen abundance relative to the other two BPT diagrams. In Section 3, we have seen that star-forming outflows are clearly identified in the [S II]- and [O II]-BPT diagrams, whilst in the [N II]-BPT diagram, they are located primarily in the 'composite' region. Therefore, studies based only on the [N II]-BPT diagnostics may have misidentified the excitation of galactic outflows. For instance, Leung et al. (2017) classify the outflows of 13 AGNs at z $\sim$ 2 only based on the [N II]-BPT diagram; about half of these outflows are located in the 'composite' region of the [N II]-BPT diagram; hence, these outflows could be hosting star formation, similarly to the outflows investigated in this paper.

Another problem is that in many spectroscopic surveys outflows are searched through blue wings of the [O III]5007 line. Because of the dominance of this line in AGN-driven outflows, as discussed above, many of these surveys have certainly biased their search towards outflows whose diagnostics are AGN dominated.

Finally, with the growing interest in studying local galaxy outflows in much greater details thanks to improved, high sensitivity and wider field of view integral field spectrometers (e.g. MUSE at the VLT), alongside evidence for star formation being found in additional individual outflows studied in detail (Venturi et al. in preparation; Fluetsch et al. in preparation; Maiolino et al. 2017), we expect to see many highly detailed and successful studies of star formation within outflows within the years to come.

7 IMPLICATIONS FOR GALAXY EVOLUTION

Stars formed in galactic outflows have completely different dynamical properties relative to the stars forming in galactic discs. Indeed, as soon as stars form in the outflow they only respond to gravity, hence moving ballistically. If the velocity at the time of formation inside the outflow exceeds the escape velocity then the newly formed stars will leave the galaxy and disperse in the IGM. If the velocity is lower than the escape velocity then the newly formed stars will be bound; they will be rapidly decelerated and will start oscillating around the galactic centre. The latter is also one of the reasons why it is difficult to identify the young stars formed in the outflows, since as soon as they form they decouple from the outflow and their velocity is quickly reduced (within a few Myr, Maiolino et al. 2017) becoming kinematically difficult to distinguish from the stars in the disc.

In the case of the stars formed in the outflows that are gravitationally bound, their resulting orbits may predominantly be radial. However, as shown in Maiolino et al. (2017) for the specific case of IRAS F23128-5919, the gravitational interaction with the galactic disc, or any other non-spherically symmetric potential (stellar bar, flyby galaxies) will introduce a tangential component to the stellar velocities, hence randomizing their orbits. Moreover if the expelled gas was initially in rotation around the galactic centre, then the resulting stars formed in the outflow star can also preserve some minor rotation component.

What is the primary fate of stars formed in the outflow has still to be investigated properly in a statistical way. Models expect both scenarios, i.e. escaping and gravitationally bound, depending on the nature and properties of the outflow (Zubovas et al. 2013c). In the case of the star-forming outflow in IRAS F23128-5919, which has been studied in great detail, Maiolino et al. (2017) has shown that most of the stars born in the outflow are gravitationally bound. A detailed study of both the MaNGA galaxies shown here (as well as those for which a BPT analysis has not been possible) is postponed to a later paper; however, a rough analysis of the kinematics and of the galaxy dynamics suggest a broad range of possibilities, from stars on close, gravitationally bound orbits to stars escaping the galaxy potential.

In either case, the fact that star formation in outflows has been found by us to be so common implies that this newly discovered phenomenon may have major implications for galaxy evolution and even result into a paradigm change in some specific areas. In the following, we discuss some of the potential implications of star formation in outflows for galaxy evolution and to explain some of the galactic properties.

7.1 Formation of the spheroidal component of galaxies

If stars formed in outflows are gravitationally bound (this seems to be the case in most cases, as the broad component velocity dispersion is generally comparable or slightly lower than the escape velocity, as expected by some models, Zubovas et al. 2013a), then they can contribute significantly to the formation and evolution of the spheroidal component of galaxies, i.e. bulge, halo, and even contribute to the formation of elliptical galaxies. Indeed, Silk (2013) have proposed that such positive feedback mechanism may explain some of the extreme star-forming galaxies at high redshift, which are thought to be progenitors of local ellipticals. Ishibashi et al.

(2013) have even suggested that star formation in AGN-driven outflows can contribute to the observed size evolution of elliptical galaxies across the cosmic epochs. Wang & Loeb (2018) have also suggested that the double shells often observed in elliptical galaxies, typically ascribed to merging events, can actually be the result of star formation in outflows.

The integrated spectra of local elliptical galaxies does not seem to show evidence a large fraction of stars on radial orbits (Cappellari et al. 2007). However, the study of Cappellari et al. (2007) of 24 local elliptical galaxies results into a radial anisotropy parameter $\beta_r > 0$ (i.e. preference for radial orbits) in ∼2/3 of their sample. The kinematics of individual stars would be needed to properly assess the fraction of the radial orbits.

For galactic bulges and galactic haloes, for which star formation within outflows is likely more important, a similar analysis on the distribution of radial and tangential orbits has not yet been performed to our knowledge. It is however interesting to note that recent studies of the stellar velocity distribution in the 5 kpc around the Sun, based on Gaia data, have revealed a significant population of stars with highly radial galactocentric orbits (Belokurov et al. 2018; Myeong et al. 2018). The second *Gaia* data release is expected to further expand the characterization and detection of stars on radial orbits.

Within this context star formation in outflows has also been invoked to explain the population of hypervelocity stars in the Galactic halo (Silk & Mamon 2012; Zubovas et al. 2013c; Wang & Loeb 2018).

7.2 BH–galaxy correlations

Clearly, stars formed in AGN-driven outflows can potentially directly produce the $M_{\rm BH}$–$M_{\rm spheroid}$ relation. In particular, given the correlation between outflow rate and AGN luminosity (i.e. BH accretion rate), obtained by various observational works (Fluetsch et al. 2018; Fiore et al. 2017; Cicone et al. 2014), and assuming the correlation between outflow rate and star formation in the outflow found in Section 4.3 (Figs 10 and 11) holds true for all AGN-driven outflows, it is clear that the combination of the two can result into a correlation between BH mass and stars formed in the outflows.

Quantifying the expected relation is yet not simple, as different authors have found different scaling relations between ionized outflows and AGN luminosity (Fiore et al. 2017; Fluetsch et al. 2018). However, if we consider the compilation by Fiore et al. (2017) (where the correlation between ionized outflow rate and AGN luminosity is slightly superlinear), and assume an AGN radiative efficiency of 0.1, then the relation between AGN luminosity and ionized outflow rate translates into

$$\log\left(\dot{M}_{\rm outf\text{-}ion}\right) = 0.85 + 1.29\log\left(\dot{M}_{\rm BH}\right), \quad (8)$$

where both the ionized outflow rate and BH accretion rate are in units of $\rm M_\odot\ yr^{-1}$, and where we have corrected the outflow rates estimated by Fiore et al. (2017) (specifically by a factor of three) to account for the different assumptions to derive the outflow rate in our work. Combining equation (8) with the relation between ionized outflow rate and star formation in the outflow, i.e. equation (2) gives

$$\rm SFR_{outf\text{-}ion} = 15\left(\dot{M}_{\rm BH}\right)^{1.56}, \quad (9)$$

where $\rm SFR_{outf\text{-}ion}$ is the SFR inside the outflow, again in units of $\rm M_\odot\ yr^{-1}$. The relation is superlinear. At low/intermediate accretion rates ($\dot{M}_{\rm BH} < 5\,\rm M_\odot\ yr^{-1}$), the relation gives a $\rm SFR/\dot{M}_{BH}$ ratio lower than the observed local bulge-to-black hole mass ratio, i.e. $M_{\rm bulge}/M_{\rm BH} \sim 200$ (Kormendy & Ho 2013), whilst at high accretion rates ($\dot{M}_{\rm BH} > 5\,\rm M_\odot\ yr^{-1}$) the implied $\rm SFR/\dot{M}_{BH}$ ratio is higher than the local bulge-to-black hole mass ratio. This behaviour in two different regimes can potentially explain the very low $\rm M_{star}/M_{BH} \sim 30$ observed at high redshift (e.g. Wang et al. 2013; Decarli et al. 2018), which can be reached through the first (low accretion rate) regime, in which the BH forms faster than the stellar population (relative to the local relation), whilst later (in the high accretion rate regime) the implied higher star formation in the outflow can enable the galaxy to build up quickly enough stellar mass to reach the local relation.

Of course, due to the relations being non-linear and the correlations not yet well established, more work is needed to properly assess exactly whether the BH–galaxy correlations and their evolution can be fully explained through star formation in outflows or not.

It is finally interesting to note that Fiore et al. (2017) and Bischetti et al. (2018) have identified a very steep relationship between outflow velocity and AGN luminosity. More specifically, the outflow velocity (combining molecular and ionized outflows) scales with AGN luminosity, i.e. BH accretion rate, as

$$L_{\rm AGN} \propto v_{\rm outfl}^{4.6}. \quad (10)$$

The slope of this correlation is comparable to the slope of the correlation between BH mass and stellar velocity dispersion:

$$M_{\rm BH} \propto \sigma_v^{4.5-5} \quad (11)$$

(e.g. Shankar et al. 2016). Therefore, if during the active outflow phases BHs are accreting close to the Eddington limit (hence $L_{\rm AGN} \propto M_{\rm BH}$), as expected by many outflow models (King & Pounds 2015), and stars form inside such AGN-driven outflows, then the stellar velocity dispersion of the resulting spheroidal stellar component would have a velocity dispersion consistent with that of the $M_{\rm BH}$–σ relation.

7.3 Extragalactic supernovae, CGM/IGM *in situ* enrichment, and halo heating

The population of stars formed in galactic outflows can result in supernovae (SNe) exploding on large orbits, outside the galaxy. As discussed in the previous sections most of the stars formed in the outflow are rapidly decelerated (within a few Myr) and will quickly fall back on to the galaxy, hence a significant fraction of the associated SNe explode close to the galaxy. However, a fraction of stars in the outflow may have larger orbits or even escape the galaxy, as expected in models (Zubovas et al. 2013c) and as observed (Maiolino et al. 2017). The resulting SNe should appear as SNe exploding outside galaxies.

Search for SNe tends to be biased towards SNe exploding inside galaxies, as monitoring and follow-up are typically focused on galaxies. However, hostless or intergalactic SNe have been observed in clusters (Gal-Yam et al. 2003; Graham et al. 2015; Gupta et al. 2016).

It should be reminded that locally star formation in outflows is a relatively mild phenomenon; hence, SNe outside galaxies are not expected to be very common. However, at high z, where this phenomenon is expected to be much more prominent, SNe exploding in the CGM or even in the IGM should have been much more common. Such extragalactic SNe would have directly enriched, *in situ*, the CGM and IGM, relaxing the need of metals to be expelled from galaxies through winds.

An additional implication is that SNe in the halo would be expanding in a very low-density environment, hence releasing most of the energy to the halo (in contrast to galactic SNe, which explode in dense environments hence losing most of their energy through radiative losses, Walch & Naab 2015). As a consequence, SNe outside the galaxy can be very effective in heating the halo, hence suppressing the accretion of cold gas on to the galaxy, resulting in a delayed ('preventive') feedback, which may result in quenching star formation as a consequence of starvation. Therefore, whilst galactic outflows have a positive initial effect, resulting in new stars born in the outflow, eventually they may actually have a net negative feedback effect on the entire galaxy through halo heating and galaxy starvation.

7.4 Reionization of the Universe

As discussed above, as soon as stars form in the outflow they only respond to gravity, hence they quickly decouple from the outflowing clouds (which are instead also subject to radiation pressure, ram pressure, and other fluidodynamic effects). As a consequence, the massive young, hot stars formed in the outflow will have very high escape fraction of ionizing photons. Therefore, if this phenomenon is taking place in the early Universe, star formation in outflows can greatly contribute to the reionization of the Universe. Indeed, one of the main problems of current theories is that the ionizing photons escape fraction typically observed in galaxies is very low (less than 5–10 per cent), making it difficult for models to account for the reionization of the Universe. The large escape fraction expected for stars formed in outflows may help to tackle this long-standing issue.

8 CONCLUSIONS

Several models have proposed that massive galactic outflows may form stars inside them, with potentially far reaching implications as stars formed inside outflows would have completely different kinematic properties than those formed in galactic discs. The detection of large amounts of molecular gas, both dense and clumpy, in galactic outflows does indeed support the scenario that galactic outflows should form stars. However, direct evidence of star formation inside galactic outflows was so far found only in a single galaxy, leaving unclear whether this is a rare phenomenon or common to galactic outflows.

In order to address this issue, we have analysed integral field spectroscopic data of 2800 local galaxies in the MaNGA DR2. Through a detailed spectral analysis, we have identified a sample of 37 galaxies that shows clear evidence for outflows and whose excitation mechanism can be investigated through the detection of multiple nebular lines, which can be used to trace the excitation of outflowing gas through the BPT diagnostic diagrams.

We have obtained the following results:

(i) About 30 per cent of the outflows have BPT diagnostic diagrams consistent with being star forming; that is, the nebular lines in the outflow are primarily excited by the UV radiation of young hot stars. Moreover, we find that half of the outflows show at least some fraction of them (>10 per cent) being excited by star formation. These results highlight that star formation is common in a large fraction of galactic outflows.

(ii) The analysis of the ionization parameter in the star-forming outflows, which is indistinguishable from (or even higher than) normal star-forming regions, confirms that the outflowing gas is not photoionized by the UV radiation coming from the underlying galactic discs, but must be photoionized by *in situ* (i.e. within the outflow) star formation.

(iii) In these local galaxies, the star formation inside the outflow generally accounts only for about 5–30 per cent of the total star formation in the galaxy. However, star formation inside the outflow can contribute significantly, or even dominate star formation in the central few kpc.

(iv) We find that, for those galaxies whose outflow is dominated by star formation, the SFR inside the outflows correlates with the ionized outflow rate. If extrapolated to the outflow rates observed in distant massive galaxies and quasars, then the implied SFR inside those outflows can be up to several 100 $M_{\odot}$ yr^{-1}, hence potentially contributing significantly to the evolution of galaxies. We suggest that evidence for star formation in the outflows of distant galaxies may already be present.

(v) We show that galaxies with star formation inside the outflow are primarily distributed along the 'main sequence' (or, in some cases, slightly above it) and are typically isolated, regular disc galaxies.

(vi) We discuss the possible reasons why star formation may have remained elusive until recently. We show that even if prominent star formation is present inside the outflow, the presence of an even faint AGN generally dominates the diagnostics. This may have precluded the detection of star formation in many outflows, especially in integrated spectra or with poor spatial resolution. We also point out that outflows identified through the [O III]5007 line may have biased the samples against those dominated by star formation. Moreover, the use of the [N II]-BPT diagnostic diagram may also have resulted in improperly classifying the nature of some outflows.

(vii) As soon as stars form inside galactic outflows they react only to gravity, they decouple from the gaseous outflow and move ballistically. Stars formed in galactic outflows may be either escape the galaxy, or remain gravitationally bound. As our study has revealed that star formation inside galactic outflows is a relatively common phenomenon, we have discussed the implications of such widespread production of stars with kinematic properties completely different from those formed in galactic discs. Specifically:

(a) Star formation inside outflows can potentially contribute significantly to the formation of the spheroidal component of galaxies (bulge, halo, and possibly also part of elliptical galaxies). Within this context, stars formed inside galactic outflows can explain the population of stars on radial orbits recently discovered in our Galaxy, as well as the population of hypervelocity stars. The same phenomenon can explain she double-shells observed in elliptical galaxies.

(b) This phenomenon can contribute to establish the correlations between BHs and their host galaxies, and in particular the M_{BH}–σ and the M_{BH}–$M_{spheroid}$ relations.

(c) Stars formed in galactic outflows and escaping the galaxy would produce SNe exploding outside galaxies, hence accounting for the population of hostless SNe observed in galaxy cluster. SNe exploding on large orbits, or outside galaxies, can contribute to the *in situ* enrichment of the CGM and of the IGM. Such SNe can also result in a very effective heating of the galactic halo, hence preventing cold gas accretion on to the galaxy and therefore contributing to the delayed quenching of star formation in the galaxy as a consequence of starvation.

(d) Young stars formed in the outflow quickly decouple from their molecular cloud and therefore are expected to have large escape fraction of ionizing photons. As a consequence, if star

formation in outflows is common to primeval galaxies, this phenomenon can contribute significantly to the reionization of the Universe.

ACKNOWLEDGEMENTS

The authors are grateful to the anonymous referee for their very useful comments and suggestions, which really improved the manuscript. The authors are also grateful to Andy Fabian, Stijn Wuyts, Alessandro Marconi, Tiago Costa, and Kastytis Zubovas for their useful comments. RG and RM acknowledge European Research Council (ERC) Advanced Grant 695671 'QUENCH' and support by the Science and Technology Facilities Council (STFC). RR thanks to CNPq and FAPERGS for partial funding this project. Funding for the SDSS-IV has been provided by the Alfred P. Sloan Foundation, the U.S. Department of Energy Office of Science, and the Participating Institutions. SDSS acknowledges support and resources from the Center for High-Performance Computing at the University of Utah. The SDSS web site is www.sdss.org.

REFERENCES

Aalto S., Garcia-Burillo S., Muller S., Winters J. M., van der Werf P., Henkel C., Costagliola F., Neri R., 2012, A&A, 537, A44
Aalto S. et al., 2015, A&A, 574, A85
Allen M. G., Groves B. A., Dopita M. A., Sutherland R. S., Kewley L. J., 2008, ApJS, 178, 20
Arribas S., Colina L., Bellocchi E., Maiolino R., Villar-Martín M., 2014, A&A, 568, A14
Baldwin J. A., Phillips M. M., Terlevich R., 1981, PASP, 93, 5
Baskin A., Laor A., 2005, MNRAS, 358, 1043
Baug T. et al., 2018, ApJ, 852, 119
Belfiore F. et al., 2016, MNRAS, 461, 3111
Bellocchi E., Arribas S., Colina L., Miralles-Caballero D., 2013, A&A, 557, A59
Belokurov V., Erkal D., Evans N. W., Koposov S. E., Deason A. J., 2018, MNRAS, 478, 611
Bertola F., Cinzano P., Corsini E. M., Rix H.-W., Zeilinger W. W., 1995, ApJ, 448, L13
Bicknell G. V., Sutherland R. S., van Breugel W. J. M., Dopita M. A., Dey A., Miley G. K., 2000, ApJ, 540, 678
Bieri R., Dubois Y., Silk J., Mamon G. A., Gaibler V., 2016, MNRAS, 455, 4166
Bischetti M., Maiolino R., Fiore S. C. F., Piconcelli E., Fluetsch A., 2018, preprint (1806.00786)
Blanton M. R. et al., 2017, AJ, 154, 28
Borguet B., Edmonds D., Arav N., Dunn J., Kriss G. A., 2012, ApJ, 751, 107
Brand J., Massi F., Zavagno A., Deharveng L., Lefloch B., 2011, A&A, 527, A62
Brinchmann J., Charlot S., White S. D. M., Tremonti C., Kauffmann G., Heckman T., Brinkmann J., 2004, MNRAS, 351, 1151
Bundy K. et al., 2015, ApJ, 798, 7
Calzetti D., Armus L., Bohlin R. C., Kinney A. L., Koornneef J., Storchi-Bergmann T., 2000, ApJ, 533, 682
Cappellari M., 2017, MNRAS, 466, 798
Cappellari M. et al., 2007, MNRAS, 379, 418
Carniani S. et al., 2015, A&A, 580, A102
Cazzoli S., Arribas S., Maiolino R., Colina L., 2016, A&A, 590, A125
Cicone C. et al., 2014, A&A, 562, A21
Cicone C. et al., 2015, A&A, 574, A14
Cid Fernandes R., Stasińska G., Mateus A., Vale Asari N., 2011, MNRAS, 413, 1687
Combes F. et al., 2014, A&A, 564, C1
Corsini E. M. et al., 1999, A&A, 342, 671
Cresci G. et al., 2015a, ApJ, 799, 82
Cresci G. et al., 2015b, A&A, 582, A63
Crockett R. M. et al., 2012, MNRAS, 421, 1603
Croft S. et al., 2006, ApJ, 647, 1040
Decarli R. et al., 2018, ApJ, 854, 97
Deharveng L. et al., 2015, A&A, 582, A1
Dewangan L. K., Ojha D. K., 2013, MNRAS, 429, 1386
Dewangan L. K., Ojha D. K., Anandarao B. G., Ghosh S. K., Chakraborti S., 2012, ApJ, 756, 151
Diniz S. I. F., Pastoriza M. G., Hernandez-Jimenez J. A., Riffel R., Ricci T. V., Steiner J. E., Riffel R. A., 2017, MNRAS, 470, 1703
Drory N. et al., 2015, AJ, 149, 77
Dugan Z., Bryan S., Gaibler V., Silk J., Haas M., 2014, ApJ, 796, 113
Duronea N. U., Cappa C. E., Bronfman L., Borissova J., Gromadzki M., Kuhn M. A., 2017, A&A, 606, A8
Dwarkadas V. V., Dauphas N., Meyer B., Boyajian P., Bojazi M., 2017, ApJ, 851, 147
Díaz A. I., Castellanos M., Terlevich E., Luisa García-Vargas M., 2000, MNRAS, 318, 462
El-Badry K., Wetzel A., Geha M., Hopkins P. F., Kereš D., Chan T. K., Faucher-Giguère C.-A., 2016, ApJ, 820, 131
Elbaz D., Jahnke K., Pantin E., Le Borgne D., Letawe G., 2009, A&A, 507, 1359
Fabian A. C., 2012, ARA&A, 50, 455
Feruglio C., Maiolino R., Piconcelli E., Menci N., Aussel H., Lamastra A., Fiore F., 2010, A&A, 518, L155
Figueira M. et al., 2017, A&A, 600, A93
Finn C. W. et al., 2014, MNRAS, 440, 3317
Fiore F. et al., 2017, A&A, 601, A143
Fluetsch A. et al., 2018, MNRAS, 483, 4586
Gaibler V., Khochfar S., Krause M., Silk J., 2012, MNRAS, 425, 438
Gal-Yam A., Maoz D., Guhathakurta P., Filippenko A. V., 2003, AJ, 125, 1087
Garcia-Burillo S. et al., 2015, A&A, 580, A35
Genzel R. et al., 2014, ApJ, 796, 7
Graham M. L., Sand D. J., Zaritsky D., Pritchet C. J., 2015, ApJ, 807, 83
Granato G. L., De Zotti G., Silva L., Bressan A., Danese L., 2004, ApJ, 600, 580
Gunn J. E. et al., 2006, AJ, 131, 2332
Gupta R. R. et al., 2016, AJ, 152, 154
Heckman T. M., Armus L., Miley G. K., 1987, AJ, 93, 276
Ho L. C., Filippenko A. V., Sargent W. L. W., 1993, ApJ, 417, 63
Ishibashi W., Fabian A. C., 2012, MNRAS, 427, 2998
Ishibashi W., Fabian A. C., 2014, MNRAS, 441, 1474
Ishibashi W., Fabian A. C., Canning R. E. A., 2013, MNRAS, 431, 2350
Kauffmann G. et al., 2003, MNRAS, 346, 1055
Kennicutt R. C., Evans N. J., 2012, ARA&A, 50, 531
Kewley L. J., Dopita M. A., Sutherland R. S., Heisler C. A., Trevena J., 2001, ApJ, 556, 121
Kewley L. J., Groves B., Kauffmann G., Heckman T., 2006, MNRAS, 372, 961
King A., Pounds K., 2015, ARA&A, 53, 115
King A. R., 2010, MNRAS, 402, 1516
Kormendy J., Ho L. C., 2013, ARA&A, 51, 511
Lacy M., Croft S., Fragile C., Wood S., Nyland K., 2017, ApJ, 838, 146
Ladeyschikov D. A., Sobolev A. M., Parfenov S. Y., Alexeeva S. A., Bieging J. H., 2015, MNRAS, 452, 2306
Law D. R. et al., 2015, AJ, 150, 19
Law D. R. et al., 2016, AJ, 152, 83
Leslie S., Rich J., Kewley L., Dopita M., 2014, MNRAS, 444, 1842
Leung G. C. K. et al., 2017, ApJ, 849, 48
Lim B. et al., 2018, MNRAS, 477, 1993
Maiolino R. et al., 2017, Nature, 544, 202
Marconi A., Risaliti G., Gilli R., Hunt L. K., Maiolino R., Salvati M., 2004, MNRAS, 351, 169
Martinsson T. P. K., Verheijen M. A. W., Westfall K. B., Bershady M. A., Schechtman-Rook A., Andersen D. R., Swaters R. A., 2013, A&A, 557, A130
Masters D., Faisst A., Capak P., 2016, 828, 18

Molnár D. C., Sargent M. T., Elbaz D., Papadopoulos P. P., Silk J., 2017, MNRAS, 467, 586
Monreal-Ibero A., Arribas S., Colina L., Rodríguez-Zaurín J., Alonso-Herrero A., García-Marín M., 2010, A&A, 517, A28
Morselli L., Popesso P., Erfanianfar G., Concas A., 2017, A&A, 597, A97
Mukherjee D., Bicknell G. V., Wagner A. Y., Sutherland R. S., Silk J., 2018
Myeong G. C., Evans N. W., Belokurov V., Sanders J. L., Koposov S. E., 2018, ApJ, 856, L26
Nagao T., Maiolino R., Marconi A., 2006, A&A, 459, 85
Nayakshin S., Zubovas K., 2012, MNRAS, 427, 372
Pereira-Santaella M. et al., 2016, A&A, 594, A81
Perna M., Lanzuisi G., Brusa M., Cresci G., Mignoli M., 2017, A&A, 606, A96
Piqueras López J., Colina L., Arribas S., Alonso-Herrero A., Bedregal A. G., 2012, A&A, 546, A64
Privon G. C. et al., 2017, ApJ, 835, 213
Rees M. J., 1989, MNRAS, 239, 1P
Renzini A., Peng Y.-j., 2015, ApJ, 801, L29
Sakamoto K., Aalto S., Combes F., Evans A., Peck A., 2014, ApJ, 797, 90
Salomé Q., Salomé P., Combes F., 2015, A&A, 574, A34
Santoro F., Oonk J. B. R., Morganti R., Oosterloo T. A., Tadhunter C., 2016, A&A, 590, A37
Sarzi M. et al., 2006, MNRAS, 366, 1151
Sarzi M. et al., 2010, MNRAS, 402, 2187
Shankar F. et al., 2016, MNRAS, 460, 3119
Silk J., 2013, ApJ, 772, 112
Silk J., Mamon G. A., 2012, RAA, 12, 917
Strom A. L., Steidel C. C., Rudie G. C., Trainor R. F., Pettini M., 2018, ApJ, 868, 117
Strom A. L., Steidel C. C., Rudie G. C., Trainor R. F., Pettini M., Reddy N. A., 2017, ApJ, 836, 164
Sturm E. et al., 2011, ApJ, 733, L16
Thompson M. A., Urquhart J. S., Moore T. J. T., Morgan L. K., 2012, MNRAS, 421, 408
Ueda Y. et al., 2015, ApJ, 815, 1
Venturi G., 2018, A&A, 619, A74
Walch S., Naab T., 2015, MNRAS, 451, 2757
Walter F. et al., 2017, ApJ, 835, 265
Wang R. et al., 2013, ApJ, 773, 44
Wang X., Loeb A., 2018, New A, 61, 95
Yan R. et al., 2016a, AJ, 152, 197
Yan R. et al., 2016b, AJ, 151, 8
Young L. M., Bureau M., Cappellari M., 2008, ApJ, 676, 317
Zavagno A. et al., 2010a, A&A, 518, L101
Zavagno A. et al., 2010b, A&A, 518, L81
Zubovas K., King A. R., 2014, MNRAS, 439, 400
Zubovas K., Nayakshin S., King A., Wilkinson M., 2013a, MNRAS, 433, 3079
Zubovas K., Nayakshin S., Sazonov S., Sunyaev R., 2013b, MNRAS, 431, 793

SUPPORTING INFORMATION

Supplementary data are available at *MNRASJ* online.

Figure 4. (a) Distribution of the broad (outflow) component of the nebular lines on the BPT diagrams for the same representative galaxy of Figs 1 and 2. A significant fraction of this galactic outflow is in the BPT regions typically populated by star-forming regions and star-forming galaxies. The magenta star shows the median location of the BPT points in the outflow. The background grey-scale contours indicate the distribution of several hundred thousand galaxies in the SDSS survey. (b) Spatially resolved BPT classification of the outflowing gas, using the same colour coding as in (A). The central region of the outflow is mostly star forming, whilst towards the outer parts of the outflow excitation by shocks likely dominates. Maps for the other 37 galaxies including BPT maps for the narrow components.

Please note: Oxford University Press is not responsible for the content or functionality of any supporting materials supplied by the authors. Any queries (other than missing material) should be directed to the corresponding author for the article.

APPENDIX: SHOCK MODELS, DIAGNOSTIC DIAGRAMS AND PARAMETERS OF INDIVIDUAL GALAXIES

As mentioned in Section 3.3, we have employed MAPPINGS III library of fast radiative shock models to investigate whether the line ratios observed in star-forming outflows could be potentially explained by some form of shocks excitation. We have used the grid of shock models obtained by Allen et al. (2008), which span a broad range of velocities ($v_s = 100$–$1000\,\mathrm{km\,s^{-1}}$) and magnetic parameters ($B/\sqrt{n} = 10^{-4} - 10\,\mu\mathrm{G\,cm^{3/2}}$). We have adopted solar abundances (appropriate for the central region of these galaxies; Belfiore et al. 2016) and pre-shock densities of 1 $\mathrm{cm^{-3}}$ (which is the case most extensively studied by Allen et al. 2008 and generally regarded as appropriate for the pre-shock conditions). The resulting grids of models are plotted on the three BPT diagrams and on the R_{23} versus O_{32} diagram in Figs A1–A4, where we also overplot the line ratios observed in the Manga outflows. As already mentioned in Section 3.3, whilst shock models can reproduce LIER and AGN-like line ratios, the vast majority of outflows that we have identified as 'star forming' (blue symbols) are not consistent with the shock models.

Tables A1 and A2 provide the identification and the main physical properties of the MaNGA galaxies investigated in this paper.

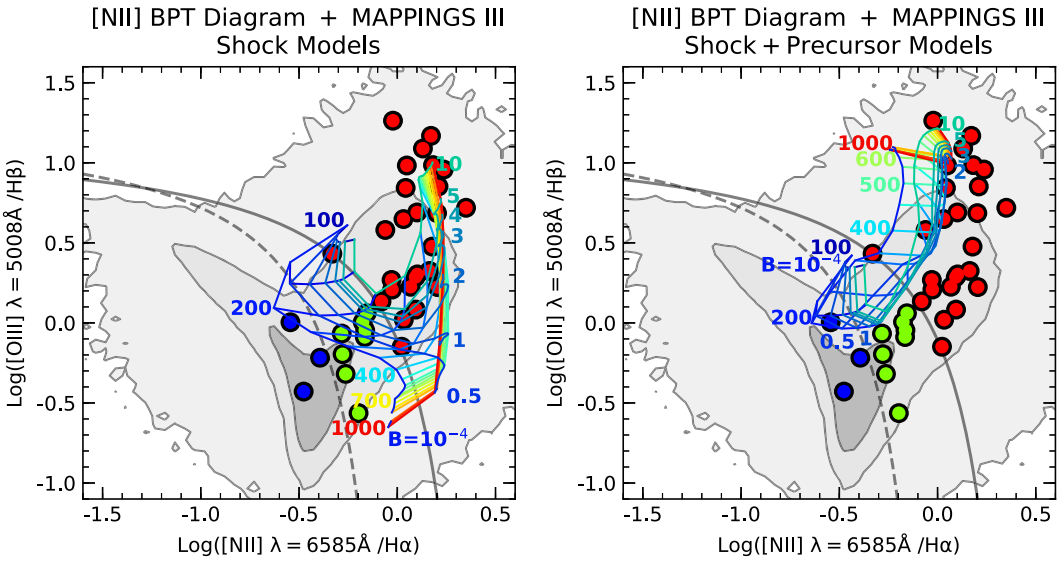

Figure A1. [N II]-BPT diagram showing the median location of the outflowing gas in each of the galaxies in our sample, as Fig. 5, but also showing the result of a grid shock models with varying velocities, from 100 km s^{-1} (blue) to 1000 km s^{-1} (red), and varying magnetic field parameter, from $B/n^{1/2} = 10^{-4}$ μG cm$^{3/2}$ (dark blue) to $B/n^{1/2} = 10$ μG cm$^{3/2}$ (light blue), both without (left) and with (right) shock precursor. Outflows classified as star forming can hardly be accounted for through shock models.

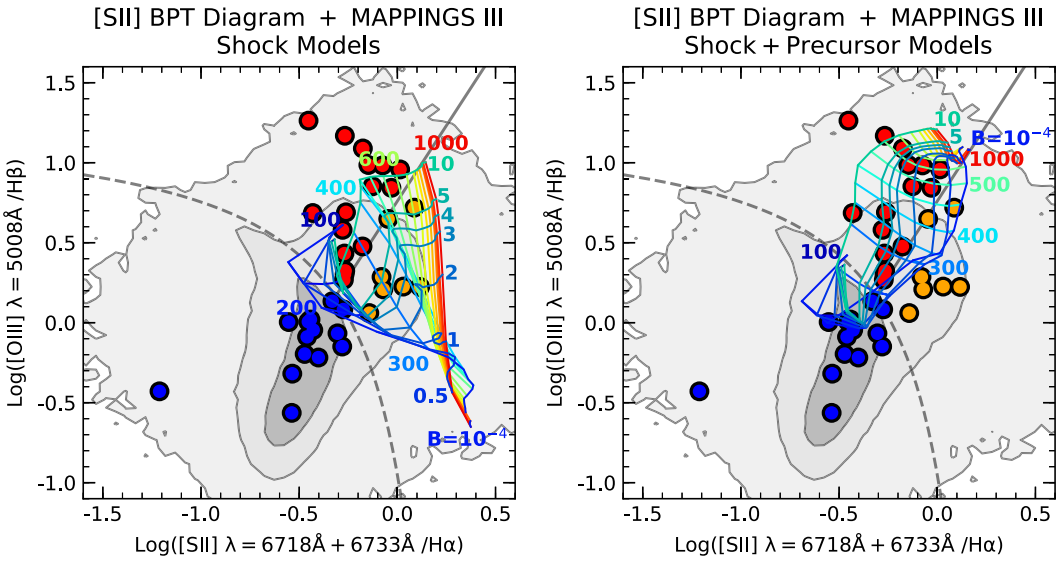

Figure A2. [S II]-BPT diagram showing the median location of the outflowing gas in each of the galaxies in our sample, as Fig. 5, but also showing the result of a grid shock models with varying velocities, from 100 km s^{-1} (blue) to 1000 km s^{-1} (red), and varying magnetic field parameter, from $B/n^{1/2} = 10^{-4}$ μG cm$^{3/2}$ (dark blue) to $B/n^{1/2} = 10$ μG cm$^{3/2}$ (light blue), both without (left) and with (right) shock precursor. Most outflows classified as star forming cannot be explained in terms of shock.

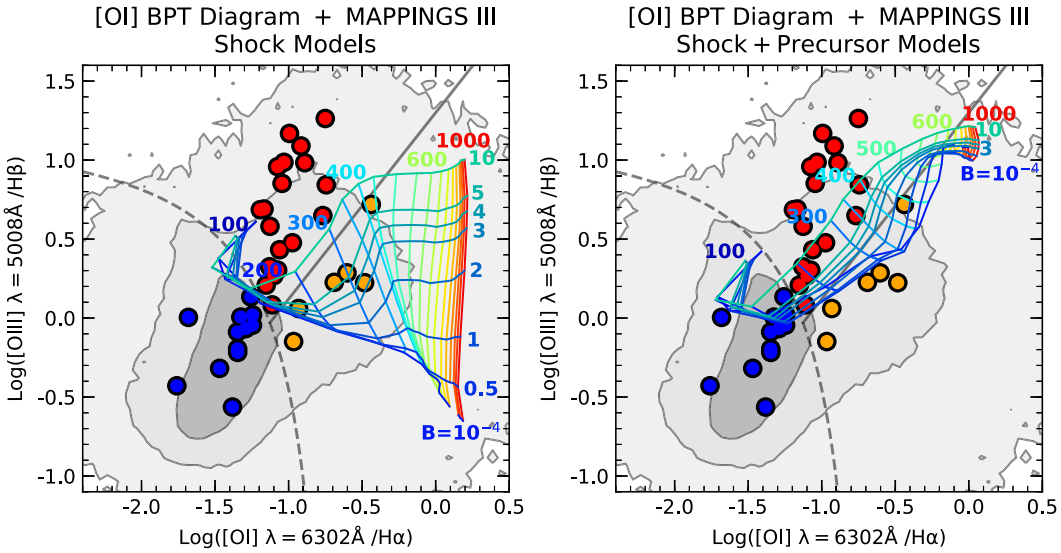

Figure A3. [O I]-BPT diagram showing the median location of the outflowing gas in each of the galaxies in our sample, as Fig. 5, but also showing the result of a grid shock models with varying velocities, from 100 km s^{-1} (blue) to 1000 km s^{-1} (red), and varying magnetic field parameter, from $B/n^{1/2} = 10^{-4}$ μG cm$^{3/2}$ (dark blue) to $B/n^{1/2} = 10$ μG cm$^{3/2}$ (light blue), both without (left) and with (right) shock precursor. Most outflows classified as star forming cannot be explained in terms of shock.

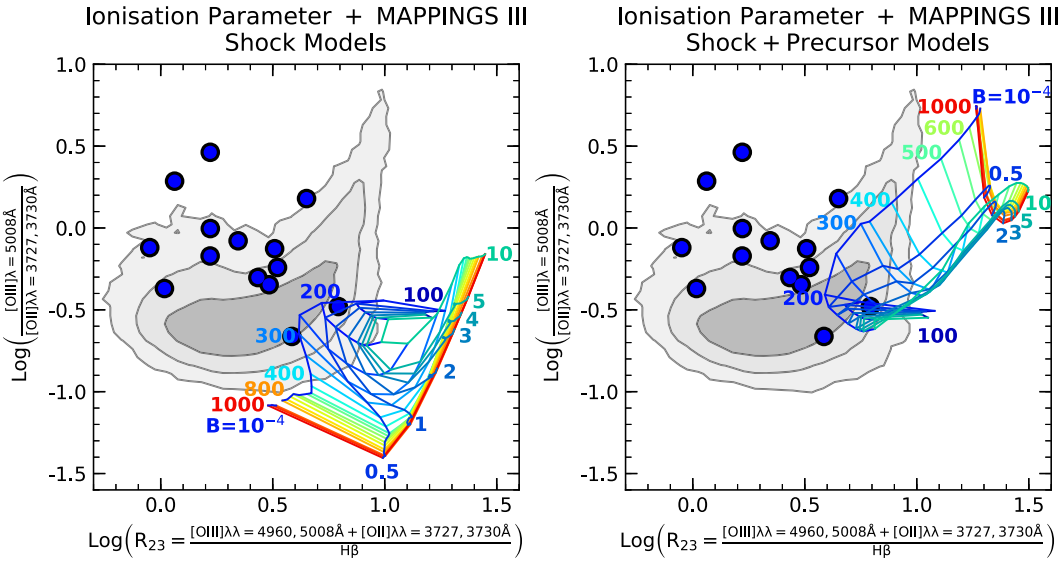

Figure A4. R_{23} versus [O III]/[O II] diagram showing the median location of the outflowing gas in each of the galaxies in our sample, as Fig. 7, but also showing the result of a grid shock models with varying velocities, from 100 km s^{-1} (blue) to 1000 km s^{-1} (red), and varying magnetic field parameter, from $B/n^{1/2} = 10^{-4}$ μG cm$^{3/2}$ (dark blue) to $B/n^{1/2} = 10$ μG cm$^{3/2}$ (light blue), both without (left) and with (right) shock precursor. Most outflows classified as star forming cannot be explained in terms of shock.

Table A1. List of MaNGA galaxies whose outflow can be characterized through the BPT diagrams. The columns provide the following information: (1) plate ID; (2) IFU ID; (3) right ascension; (4) declination; (5) stellar mass taken from the MPA-JHU catalogue (Brinchmann et al. 2004) (lack of entry means that the stellar mass is not available in the MPA-JHU catalogue).

PID	IFU	RA (deg)	Dec. (deg)	z	$\log(M_{star})$ ($M_\odot$)
7443	12703	229.52558	42.74584	0.04027	10.82[a]
8241	6102	126.05963	17.33195	0.03725	10.45
8244	3702	131.81500	51.24580	0.02754	10.01
8252	1902	146.09183	47.45985	0.02589	9.35
8256	12704	166.12940	42.62455	0.12610	11.16[a]
8318	6102	197.23931	45.90544	0.12907	11.34
8329	3701	213.43219	43.66248	0.08934	–[a]
8341	12704	189.21325	45.65117	0.03034	10.62
8439	6102	142.77816	49.07974	0.03393	10.72
8482	12704	243.58182	50.46561	0.06025	11.39
8550	3704	248.42638	39.18511	0.02984	10.44
8550	9102	247.20905	39.83508	0.03585	10.67
8588	6101	248.45675	39.26320	0.03176	10.74
8612	12704	254.56457	39.39146	0.03431	10.76
8715	3702	119.92067	50.83997	0.05436	10.33
8931	9101	193.07383	27.08555	0.02098	10.25
8946	3701	168.95772	46.31956	0.05328	10.67
8948	12704	167.30601	49.51943	0.07242	11.02
8952	3703	205.44092	27.10634	0.02878	10.33
8979	6102	241.82338	41.40360	0.03463	10.76
9026	9101	249.31841	44.41822	0.03141	10.82
9049	1901	247.56097	26.20647	0.13145	11.38
10001	6102	132.65399	57.35966	0.02610	10.67
8250	12704	138.98137	44.33276	0.03978	10.95[a]
8263	3701	184.76431	46.10679	0.03856	10.09
8257	12701	165.49581	45.22802	0.01999	10.38
8464	3702	187.0635	44.45313	0.02289	–[a]
7992	6104	255.27948	64.67687	0.02713	10.21
8078	6104	42.739429	0.369408	0.04421	10.05
8082	12701	48.896456	-1.01628	0.02680	10.44
8249	3703	139.72046	45.72778	0.02643	9.79
8250	3703	139.73996	43.50057	0.04005	9.62
8262	9102	184.55356	44.17324	0.02452	10.29
8315	12705	235.92048	39.54035	0.06347	10.60
8550	12703	247.67443	40.52938	0.02981	10.55
8726	12701	115.71703	22.11273	0.02864	10.72
8931	12702	192.76494	27.36996	0.02772	10.07

[a]Interacting systems.

Table A2. Properties of the SFRs, outflow rate, and BPT classification of the discs and of the outflows. The columns provide the following information: (1) plate ID; (2) IFU ID; (3) SFR in the disc; (4) SFR in the outflow (only for those galaxies that are dominated by star formation in the outflow according to the [S II]-BPT diagram); (5) ionized outflow rate determined through the broad H α emission; (6) ionized outflow rate determined through the broad [O III] emission; (7–9) BPT classification of the nebular emission of the galaxy disc; (10–12) BPT classification of the nebular emission of the outflow.

PID	IFU	SFR (disc)	SFR (outflow)	$\dot{M}_{\rm outf}$(Ha)	$\dot{M}_{\rm outf}$([O III])	BPT class. disc			BPT class. outf		
		($M_\odot$ yr^{-1})	($M_\odot$ yr^{-1})	($M_\odot$ yr^{-1})	($M_\odot$ yr^{-1})	[N II]	[S II]	[O I]	[N II]	[S II]	[O I]
7443	12703	36.38	–	2.608	0.057	Comp	SF	LIER	AGN	AGN	AGN
8241	6102	5.21	–	0.37	0.036	Comp	SF	SF	AGN	AGN	AGN
8244	3702	1.39	–	0.09	0.004	SF	SF	SF	AGN	AGN	AGN
8252	1902	0.07	–	0.01	0.001	SF	SF	LIER	AGN	AGN	AGN
8256	12704	2.45	–	0.59	0.038	AGN	LIER	AGN	AGN	AGN	AGN
8318	6102	9.13	–	1.99	0.194	Comp	SF	AGN	AGN	LIER	LIER
8329	3701	0.85	–	0.15	0.015	Comp	SF	LIER	AGN	LIER	LIER
8341	12704	2.45	–	0.21	0.045	SF	SF	SF	AGN	AGN	AGN
8439	6102	4.98	–	0.61	0.023	Comp	SF	SF	AGN	AGN	AGN
8482	12704	1.22	–	<0.1	0.014	AGN	LIER	AGN	AGN	LIER	LIER
8550	3704	0.19	–	0.34	0.012	AGN	LIER	SF	AGN	LIER	LIER
8550	9102	4.90	–	0.07	0.004	SF	SF	SF	AGN	AGN	AGN
8588	6101	3.82	–	0.24	0.013	Comp	SF	SF	AGN	LIER	AGN
8612	12704	1.76	–	0.16	0.015	AGN	AGN	AGN	AGN	AGN	AGN
8715	3702	2.70	–	16.90	0.887	AGN	AGN	AGN	AGN	AGN	AGN
8931	9101	0.36	–	0.15	0.001	Comp	SF	LIER	AGN	AGN	AGN
8946	3701	0.51	–	0.06	0.005	Comp	SF	SF	AGN	AGN	AGN
8948	12704	4.43	–	0.17	0.013	Comp	SF	SF	AGN	AGN	AGN
8952	3703	0.24	–	0.02	0.002	Comp	SF	SF	SF	LIER	LIER
8979	6102	1.37	–	0.05	0.004	SF	SF	SF	AGN	LIER	AGN
9026	9101	1.23	–	0.20	0.008	Comp	SF	SF	AGN	AGN	AGN
9049	1901	15.24	–	0.49	0.033	Comp	SF	SF	AGN	AGN	AGN
10001	6102	1.17	–	0.24	0.004	Comp	SF	SF	AGN	AGN	AGN
8250	12704	16.57	4.30	0.33	0.009	Comp	SF	SF	AGN	SF	AGN
8263	3701	0.61	0.31	0.13	0.003	Comp	SF	SF	AGN	SF	LIER
8257	12701	5.824	0.64	0.22	0.016	Comp	SF	SF	AGN	SF	SF
8464	3702	2.20	0.17	0.12	0.010	Comp	SF	SF	AGN	SF	SF
7992	6104	2.86	0.29	0.09	0.003	Comp	SF	SF	Comp	SF	SF
8082	12701	1.10	0.09	0.06	0.004	SF	SF	SF	Comp	SF	SF
8262	9102	5.00	0.93	0.36	0.051	SF	SF	SF	Comp	SF	SF
8315	12705	5.74	1.04	0.26	0.021	SF	SF	SF	Comp	SF	SF
8550	12703	1.11	0.09	0.04	0.004	SF	SF	SF	Comp	SF	SF
8726	12701	0.93	0.23	0.11	0.009	Comp	SF	SF	Comp	SF	SF
8931	12702	1.72	0.10	0.05	0.003	SF	SF	SF	Comp	SF	SF
8078	6104	1.32	0.88	0.24	0.027	Comp	SF	SF	SF	SF	SF
8249	3703	0.65	0.03	0.01	0.002	SF	SF	SF	SF	SF	SF
8250	3703	1.42	0.29	0.07	0.016	SF	SF	SF	SF	SF	SF

This paper has been typeset from a TEX/LATEX file prepared by the author.